# Intrinsic unfoldase/foldase activity of the chaperonin GroEL directly demonstrated using multinuclear relaxation-based NMR

David S. Libich[1], Vitali Tugarinov[1], and G. Marius Clore[2]

Laboratory of Chemical Physics, National Institute of Diabetes and Digestive and Kidney Diseases, National Institutes of Health, Bethesda, MD 20892-0520

This contribution is part of the special series of Inaugural Articles by members of the National Academy of Sciences elected in 2014.

Contributed by G. Marius Clore, May 27, 2015 (sent for review May 13, 2015)

**The prototypical chaperonin GroEL assists protein folding through an ATP-dependent encapsulation mechanism. The details of how GroEL folds proteins remain elusive, particularly because encapsulation is not an absolute requirement for successful re/folding. Here we make use of a metastable model protein substrate, comprising a triple mutant of Fyn SH3, to directly demonstrate, by simultaneous analysis of three complementary NMR-based relaxation experiments (lifetime line broadening, dark state exchange saturation transfer, and Carr–Purcell–Meinboom–Gill relaxation dispersion), that apo GroEL accelerates the overall interconversion rate between the native state and a well-defined folding intermediate by about 20-fold, under conditions where the "invisible" GroEL-bound states have occupancies below 1%. This is largely achieved through a 500-fold acceleration in the folded-to-intermediate transition of the protein substrate. Catalysis is modulated by a kinetic deuterium isotope effect that reduces the overall interconversion rate between the GroEL-bound species by about 3-fold, indicative of a significant hydrophobic contribution. The location of the GroEL binding site on the folding intermediate, mapped from $^{15}N$, $^{1}H_N$, and $^{13}C_{methyl}$ relaxation dispersion experiments, is composed of a prominent, surface-exposed hydrophobic patch.**

chaperonins | invisible states | dark state exchange saturation transfer | lifetime line broadening | relaxation dispersion

Chaperone networks have evolved to correctly fold native proteins and protect against the damaging effects of misfolding and aggregation on protein homeostasis (1, 2). The chaperonins, a ubiquitous subclass of chaperones, are barrel-shaped, multisubunit assemblies composed of two ring cavities, transiently capped by either an extrinsic cochaperone or a built-in lid domain, which assist protein folding in an ATP-dependent manner (3–6). Although the encapsulation mechanism and accompanying allosteric transitions driven by ATP have been extensively studied, the details of how chaperonins fold proteins remain elusive (3, 6, 7). Further, encapsulation does not appear to be an absolute requirement for successful re/folding (8). Moreover, hydrogen/deuterium exchange experiments on several protein substrates (9–12) and fluorescence-based refolding experiments (13) suggest that the prototypical chaperonin GroEL may possess intrinsic unfoldase activity. Here we take advantage of a monomeric, nonaggregating, well-defined system—a triple mutant of the Fyn SH3 domain that exists in dynamic equilibrium between the major native state and a sparsely populated folding intermediate (14, 15)—to directly demonstrate, using NMR relaxation-based methods (16), the ability of apo GroEL to accelerate the interconversion between these two states by almost three orders of magnitude. Simultaneous analysis of lifetime line-broadening (17), dark state exchange saturation transfer (DEST) (18), and Carr–Purcell–Meinboom–Gill (CPMG) relaxation dispersion (19) data permitted us to determine the catalytic rate constants and ascertain the location of the GroEL binding site on the folding intermediate under conditions where the population of GroEL-bound native and intermediate states is less than 1%. Further, GroEL unfoldase/foldase activity is modulated by SH3 deuteration, indicating that catalysis of the exchange reaction between folded and intermediate states involves direct interaction of the substrate with the walls of the GroEL chambers. These results provide a basis for how chaperonins, in the absence of cofactors and encapsulation, may be able to passively protect the cell from the deleterious effects of misfolded protein accumulation.

## Results and Discussion

**$^{15}N$-Relaxation–Based NMR Measurements.** The native state of the triple A39V/N53P/V55L mutant of the Fyn SH3 domain ($SH3^{mut}$) is slightly destabilized relative to the wild type ($SH3^{WT}$) such that the interconversion between native folded (F), intermediate (I), and unfolded states occurs on a timescale that is accessible to CPMG relaxation dispersion experiments (14). The equilibrium between these states is temperature dependent and at 10 °C, the temperature used in the current work, the unfolded state is undetectable and the population of the I state is ∼2.3% (14). Despite this low occupancy, a structure of the I state could be determined based on backbone chemical shifts and residual dipolar couplings derived from analysis of relaxation dispersion data (15). These studies showed that unfolding of the C-terminal strand (β8) exposes a hydrophobic patch on the surface of the SH3 domain.

To probe the interaction of the F and I states of the SH3 domain with apo GroEL we made use of three relaxation-based NMR experiments that are influenced in different ways by the rate constants for the interconversion between the species present

### Significance

Chaperones are integral components of the cellular machinery that assist protein folding and protect against misfolding and aggregation. A bottleneck in understanding how chaperones work is that the relevant functional states are too sparsely populated and dynamic to be observed using conventional biophysical methods. NMR is uniquely suited to detect and provide atomic resolution functional information on such "invisible" states. Here we quantitate the kinetics of the chaperone GroEL binding to a protein substrate that exists in a metastable equilibrium between the native state and a sparsely populated folding intermediate, under conditions where the GroEL-bound states are not directly observable. We show that in the absence of cofactors, GroEL possesses substantial intrinsic un/foldase activity that is mediated by hydrophobic interactions.

Author contributions: D.S.L., V.T., and G.M.C. designed research, performed research, analyzed data, and wrote the paper.

The authors declare no conflict of interest.

[1]D.S.L. and V.T. contributed equally to this work.

[2]To whom correspondence should be addressed. Email: mariusc@mail.nih.gov.

This article contains supporting information online at www.pnas.org/lookup/suppl/doi:10.1073/pnas.1510083112/-/DCSupplemental.

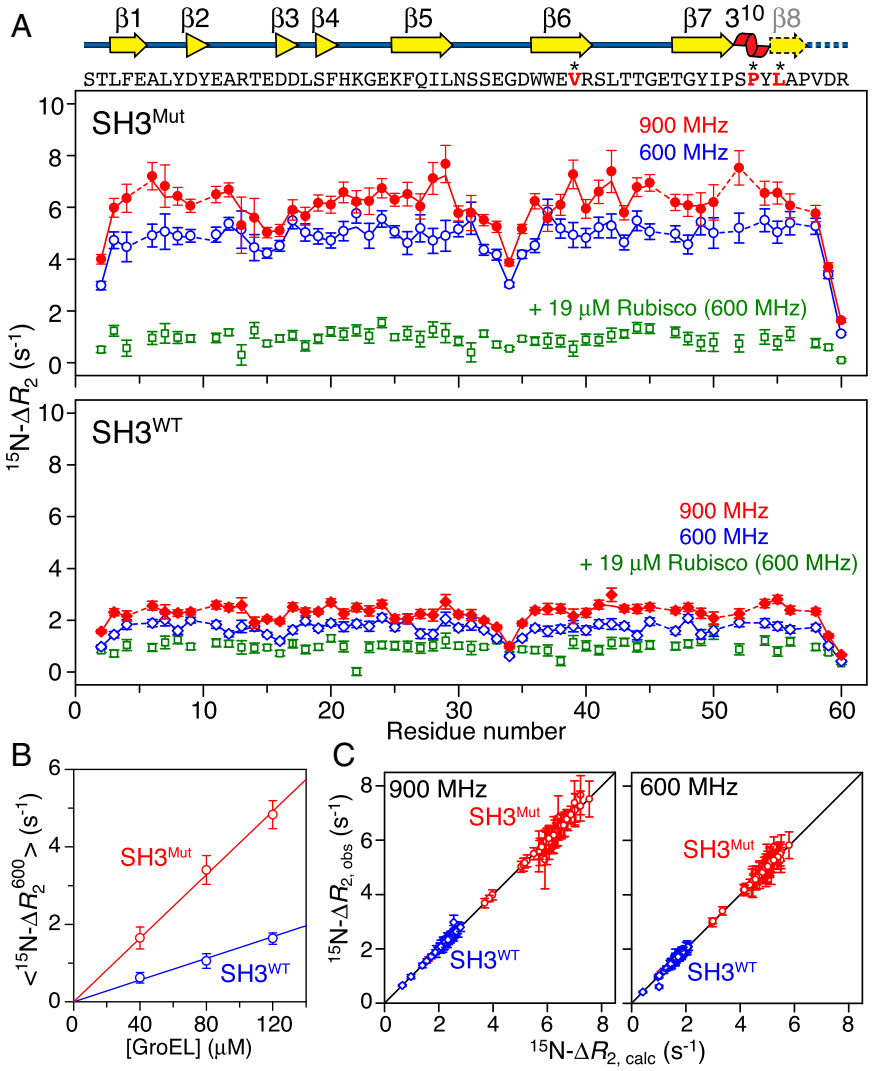


**Fig. 1.** $^{15}$N lifetime line broadening of SH3 in the presence of GroEL. (*A*) $^{15}$N-$\Delta R_2$ profiles for 100 μM $^{15}$N-labeled SH3$^{Mut}$ (*Top*) and SH3$^{WT}$ (*Bottom*) in the presence of 120 μM (in subunits) GroEL at 900 (red) MHz and 600 (blue) MHz with the experimental data shown as circles and the calculated values as lines. Also shown as controls are the $^{15}$N-$\Delta R_2$ profiles obtained upon addition of 19 μM acid-denatured Rubisco (green squares), a substrate known to bind to the internal cavity of GroEL with nanomolar affinity. This concentration corresponds to a stoichiometry of one Rubisco molecule per GroEL cavity. (*B*) Dependence of $^{15}$N-$\Delta R_2$ on concentration of GroEL for SH3$^{Mut}$ (red) and SH3$^{WT}$ (blue). (*C*) Correlation plot of observed and calculated $^{15}$N-$\Delta R_2$ values for SH3$^{Mut}$ (red) and SH3$^{WT}$ (blue) at 900 MHz (*Left*) and 600 MHz (*Right*). Experiments were conducted at 10 °C. Error bars = 1 SD.

in solution as well as by the transverse relaxation rates of these species (*SI Theory*). Both lifetime line broadening and DEST rely on large differences in transverse relaxation rates between unligated and GroEL-bound species ($^{15}$N-$R_2$ ~11 s$^{-1}$ and ~900 s$^{-1}$, respectively, at 900 MHz) (16), whereas relaxation dispersion is also dependent upon differences in chemical shifts between the interconverting states (19).

Lifetime line broadening is measured by taking the difference ($\Delta R_2$) in transverse relaxation rates ($R_2$) for the SH3 domain in the presence and absence of GroEL under conditions where chemical exchange-induced line broadening is suppressed (20) (*SI Materials and Methods*). In the presence of GroEL (120 μM in subunits), a near uniform (with the exception of the highly mobile residues at the N and C termini), field-dependent, increase in $^{15}$N-$R_2$ is observed for both $^{15}$N/protonated SH3$^{Mut}$ and SH3$^{WT}$, but the effect is about three times larger for the former than for the latter (Fig. 1*A* and Table 1). The $\Delta R_2$ effect is linearly dependent upon the concentration of GroEL (up to 120 μM in subunits; Fig. 1*B*), reflecting the linear dependence of the apparent pseudo-first-order association rate constant ($k_{on}^{app}$) on the concentration of GroEL binding sites. [Note that the increase in the $R_2$ of SH3$^{Mut}$ and SH3$^{WT}$ upon addition of GroEL is not due to an increase in viscosity as there is no detectable change in translational diffusion of the SH3 domain as measured by pulsed-field-gradient NMR (*SI Materials and Methods*).] Addition of acid-denatured ribulose-1,5-bisphosphate carboxylase (Rubisco), a substrate known to bind with nanomolar affinity to GroEL (21), essentially abolishes the effect. These observations allow one to conclude that the interactions of the I and F states with GroEL are specific and involve the interior cavity of GroEL, that the population of the GroEL-bound I state (I-G) is larger than that of the GroEL-bound F state (F-G), that the values of $k_{on}^{app}$ for the binding of F and I to GroEL are larger than $\Delta R_2^{max}$ (6.5 s$^{-1}$ at 900 MHz), and that the dissociation rate constants of F ($k'_{off}$) and I ($k_{off}$) from GroEL are comparable to or higher than the expected $^{15}$N-$R_2$ in the GroEL-bound states (~900 s$^{-1}$).

$^{15}$N-CPMG relaxation dispersion measurements on $^{15}$N/protonated SH3$^{Mut}$ reveal dispersion profiles that are modulated by GroEL (Fig. 2*A*), reflecting the interconversion between the F and

**Table 1. Average experimental values of $^{15}$N-$\Delta R_2$ and $^{13}C_{methyl}$-$\Delta R_2$ ($s^{-1}$) obtained for the $^{15}$N/protonated-SH3 and [$^{15}$N/$^1H_N$/AILV-$^{13}CH_3$]/deuterated-SH3 samples**

| Construct, field | $^{15}$N/protonated-SH3: $^{15}$N-$\Delta R_2$, $s^{-1}$ | [$^{15}$N/$^1H_N$/AILV-$^{13}CH_3$]/deuterated-SH3 | |
|---|---|---|---|
| | | $^{15}$N-$\Delta R_2$, $s^{-1}$ | $^{13}C_{methyl}$-$\Delta R_2$, $s^{-1}$ |
| SH3$^{Mut}$, 900 MHz | 6.2 ± 0.7 | 4.3 ± 0.6 | 2.4 ± 0.6* |
| SH3$^{WT}$, 900 MHz | 2.3 ± 0.3 | 2.5 ± 0.3 | 1.2 ± 0.6* |
| SH3$^{Mut}$, 600 MHz | 4.9 ± 0.5 | 3.6 ± 0.4 | 2.1 ± 0.5 |
| SH3$^{WT}$, 600 MHz | 1.7 ± 0.3 | 2.1 ± 0.2 | 1.1 ± 0.3 |

All data are reported as the mean ± SD of the obtained distributions of values. Data for residues 1, 2 and 59, 60 at the N and C termini, respectively, are excluded as these retain considerable mobility in the bound state.
*These $^{13}C_{methyl}$-$\Delta R_2$ values were measured at 800 MHz.

I states, large differences in $^{15}$N-$R_2$ between the free and GroEL-bound states of F and I, and differences in chemical shifts between the free and GroEL-bound I states. No dispersions were observed for SH3$^{WT}$ (which is known to exist in a single folded state) in the presence of GroEL, indicating that the population of the GroEL-bound state (F-G) is too small and/or that the exchange between the F and F-G states likely occurs on a timescale faster (<50 μs) than can be accessed by CPMG experiments (16, 19).

The $^{15}$N-DEST experiment involves the application of off-resonance radiofrequency (RF) radiation at a series of offsets from the resonances of the directly observable unligated F state to saturate $^{15}$N nuclei in the large, spectroscopically invisible, "dark" GroEL-bound states (I-G and F-G) (18). In the presence of GroEL, saturation of the SH3$^{Mut}$ resonances occurs far off-resonance (±15 kHz), providing information on the population of the GroEL-bound states and bound $R_2$ values (Fig. 2*B*). For SH3$^{WT}$, on the other hand, the $^{15}$N-DEST profiles in the presence of GroEL were only marginally broader than those in its absence, indicating that the population of the F-G state is extremely low and in fact can be quantified only by lifetime line broadening.

**Kinetic Analysis.** The simplest kinetic scheme that can account for the experimental NMR observations is one in which both F and I states bind to GroEL and interconversion between F and I occurs both in free solution and bound to the surface of the internal cavity of GroEL (Fig. 3). (Note that neither the $\Delta R_2$ nor the shape of the relaxation dispersion profiles in the presence of GroEL can be reproduced in the absence of direct interconversion between the F-G and I-G states) (Fig. S1). Because of the complexity of this kinetic scheme in relation to the available experimental data, two simplifying assumptions were made: (*i*) binding of state F to GroEL is the same for SH3$^{Mut}$ and SH3$^{WT}$ and can therefore be described by the lifetime line-broadening measurements carried out on SH3$^{WT}$ and (*ii*) the binding of F and I to GroEL is diffusion limited and therefore characterized by the same value of $k_{on}^{app}$. Simultaneous fitting of all of the relevant data, which include $^{15}$N-$\Delta R_2$ (Fig. 1 *A* and *C*), $^{15}$N-CPMG relaxation dispersion (Fig. 2*A*, red curves) and $^{15}$N-DEST for SH3$^{Mut}$ in the presence of GroEL (Fig. 2*B*), relaxation dispersion for SH3$^{Mut}$ in the absence of GroEL (Fig. 2*A*, blue curves), and $\Delta R_2$ for SH3$^{WT}$ (Fig. 1 *A* and *C*) (see Eq. **S4** in *SI Theory*), fully accounts for the experimental data (compare Figs. 1*C* and 2 *A* and *B*) and yields the rate constants and $^{15}$N-$R_2^{bound}$ values shown in Figs. 3 and 4*A*, respectively (see also Tables 2 and 3).

The rate constants for the interconversion of the free F and I states (Table 2) as well as the chemical shifts of the I state are in agreement with those determined previously by Kay and coworkers (14) (see Fig. S2). The value of ~60 $s^{-1}$ for $k_{on}^{app}$ corresponds to a

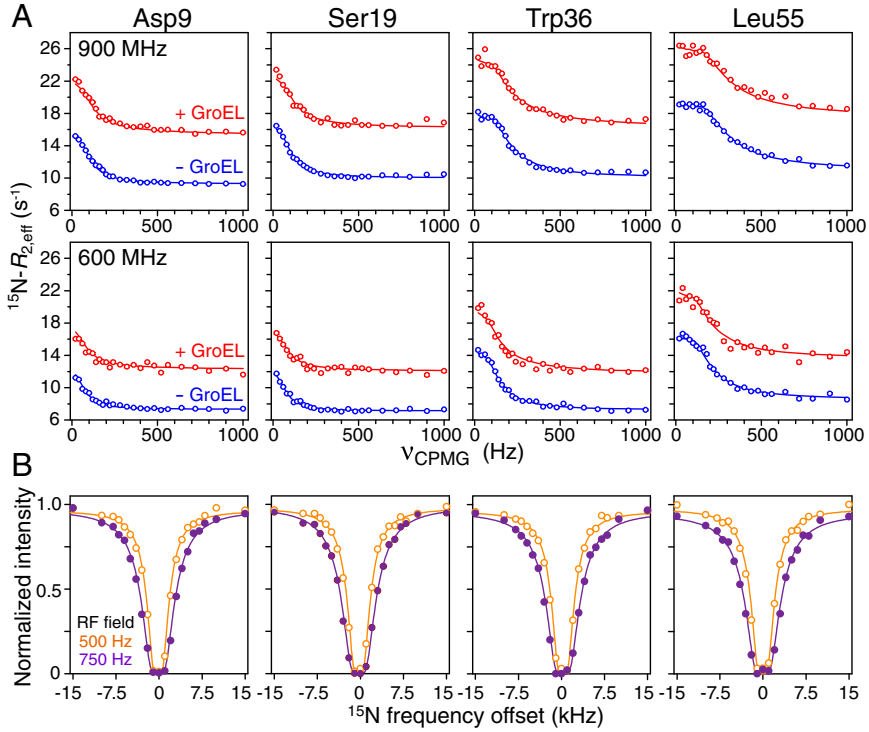


**Fig. 2.** $^{15}$N CPMG relaxation dispersion and DEST on SH3$^{Mut}$ in the presence of GroEL. (*A*) Examples of experimental (circles) and best-fit (lines) $^{15}$N CPMG relaxation profiles for SH3$^{Mut}$ (100 μM) in the presence (red) and absence (blue) of 120 μM GroEL at 900 MHz (*Top row*) and 600 MHz (*Bottom row*). (*B*) Examples of experimental (circles) and best-fit (lines) $^{15}$N-DEST profiles for SH3$^{Mut}$ in the presence of GroEL at two radiofrequency field strengths (500 Hz in orange and 750 Hz in purple) for $^{15}$N saturation. All experiments were conducted at 10 °C.

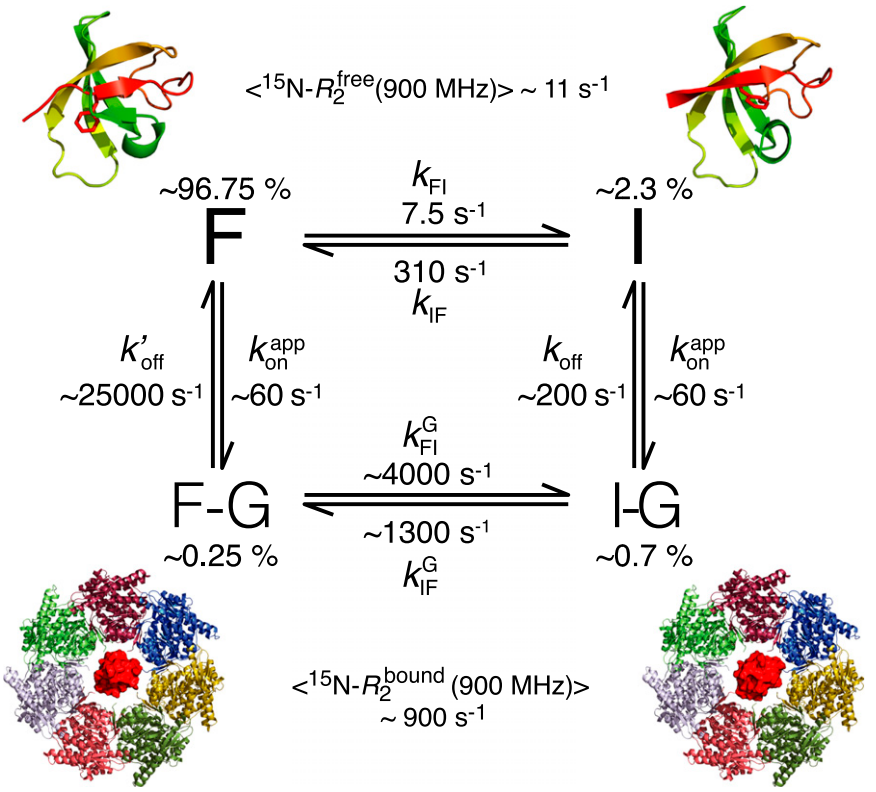


**Fig. 3.** Four-state exchange model for the interaction of $SH3^{Mut}$ with apo GroEL. F and I represent the free folded and intermediate states, respectively, of $SH3^{Mut}$ whereas F-G and I-G are the corresponding GroEL-bound states. The values of the rate constants and populations obtained for the $^{15}N$/protonated SH3 samples from the simultaneous fits to the $^{15}N$ lifetime-broadening, DEST, and CPMG relaxation dispersion data obtained at 10 °C are indicated (further details in Table 2 and *SI Theory*). The corresponding values obtained for the [$^{15}N/^{1}H_N$/AILV-$^{13}CH_3$]/deuterated SH3 samples are provided in Table 2. *Top*, ribbon diagrams of the free F [Protein Data Bank (PDB) ID: 2LP5] and I (PDB ID: 2L2P) states of $SH3^{Mut}$ together with the side chain of Phe4 (15); *Bottom*, top view of one cylinder of GroEL (32) shown as a ribbon with the seven subunits indicated by different colors and a surface representation of the SH3 domain (red) placed in the cavity, showing that there is ample room within the cavity to accommodate one SH3 molecule.

second-order association rate constant $k_{on}$ of ~$3.5 \times 10^6$ $M^{-1}{\cdot}s^{-1}$ (assuming that one SH3 molecule binds per GroEL cavity), consistent with a diffusion-limited association process for two macromolecules; the equilibrium dissociation constant ($K_D$) for the binding of I to GroEL (~60 μM) is about two orders of magnitude lower than that for F (~7 mM); and the overall exchange rate (sum of forward and backward rate constants) between the F and I states is ~20-fold faster when bound to GroEL. This is achieved by an ~500-fold acceleration of the F-G to I-G transition and a smaller ~4-fold increase in the rate constant for the reverse process. (As shown visually from the simulations in Fig. S3, the experimental relaxation dispersion profiles and $\Delta R_2$ values are consistent only with an acceleration in the interconversion between the F and I states upon GroEL binding.) Thus, apo GroEL, in the absence of any cofactors (ATP/ADP) and accessory proteins (GroES), possesses intrinsic unfoldase and foldase catalytic activity.

**$^{15}N$-Transverse Relaxation Rates in the GroEL-Bound States.** The relatively uniform $^{15}N$-$R_2^{bound}$ values derived from the fits to the data show that the I state binds to GroEL as a rigid body with the exception of the N and C termini (residues 1 and 58/59, respectively) and the loop connecting strands β5 and β6, which retain some degree of mobility on account of their significantly lower $^{15}N$-$R_2^{bound}$ values (Fig. 4*A*, and similarly for state F, see Fig. S4). The average values of the $^{15}N$-$R_2^{bound}$ rates obtained from the fits (Table 3) are consistent with the $^{15}N$-$R_2$ values estimated for an ~800-kDa complex at 10 °C at both 600-MHz and 900-MHz spectrometer fields.

**Impact of Deuteration.** To gain further insight into the catalytic activity of apo GroEL and to probe the location of the $SH3^{Mut}$ binding site, we included additional probes ($^{1}H_N$ and $^{13}C_{methyl}$ nuclei) in the analysis and recorded $^{1}H_N$, $^{15}N$, and $^{13}C_{methyl}$ CPMG relaxation dispersion experiments on a sample of $^{15}N/^{1}H_N$, AILV-$^{13}C_{methyl}$–protonated and otherwise deuterated $SH3^{Mut}$ (hereafter referred to as [$^{15}N/^{1}H_N$/AILV-$^{13}CH_3$]/deuterated-$SH3^{Mut}$) (*SI Materials and Methods*) (Fig. S5), as well as complementary $^{15}N/^{13}C_{methyl}$ $\Delta R_2$ (Fig. S6) and $^{15}N/^{13}C_{methyl}$-DEST (Fig. S7) experiments on this sample and the $SH3^{WT}$ sample with the same labeling scheme. The most significant difference with respect to the results obtained on the $^{15}N$/protonated samples of $SH3^{Mut}$ is that the $^{15}N$-$\Delta R_2$ values are decreased upon deuteration by about 40% (Table 1 and Fig. S6), indicative of a reduction in the population of the I-G state. The global fits of all of the data recorded on the mutant and wild-type [$^{15}N/^{1}H_N$/AILV-$^{13}CH_3$]/deuterated-SH3 samples to the four-state kinetic scheme of Fig. 3 (*SI Theory* and Table 2) show that the interconversion rate constants between free F to I ($k_{FI}$) are minimally affected (<25%) by deuteration, but there is an approximately twofold increase in $k_{off}$, reflecting a corresponding decrease in the affinity of the I state for GroEL. As a result, the population of the GroEL-bound I-G state is reduced to ~0.4%. In addition, $k_{FI}^{G}$ decreases a little over threefold upon deuteration of $SH3^{Mut}$ ($k_{FI}^{G}$ ~1,200 $s^{-1}$ in [$^{15}N/^{1}H_N$/AILV-$^{13}CH_3$]/deuterated-$SH3^{Mut}$) (compare Table 2). The observed decrease in $k_{FI}^{G}$ is consistent with simulations that show that reduced $^{15}N$-$\Delta R_2$ values can arise solely from a decrease in the value of $k_{FI}^{G}$ (Fig. S8). Whereas the increase in $k_{off}$ is expected if the interactions between I and GroEL are

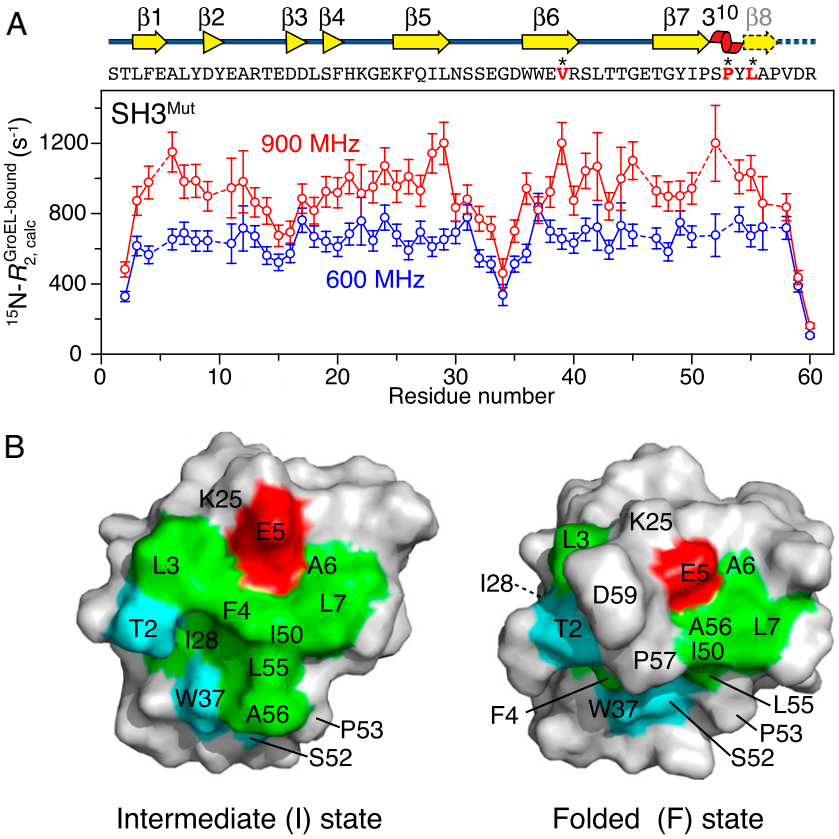


**Fig. 4.** Transverse ($R_2$) relaxation rates and chemical shifts for the intermediate (I-G) state of $SH3^{Mut}$ bound to GroEL. (*A*) Calculated $^{15}N$-$R_2^{bound}$ profiles for the I-G state at 900 (red) MHz and 600 (blue) MHz (note the lines in *A* simply serve to connect the calculated $^{15}N$-$R_2^{bound}$ values). The corresponding $^{15}N$-$R_2^{bound}$ profiles for the F-G state are shown in Fig. S4*A*. Error bars: 1 SD. (*B*) Mapping of chemical shift differences between the I-G and I states on a surface representation of the I state (*Left*) and for reference the F state (*Right*) (note the views are identical to those of the ribbon diagrams in Fig. 3, *Top*). Only residues that have a lower bound of $|\Delta\varpi^{I,I\text{-}G}| > 1.0$ ppm (E5, T14, I50, S52, L55, and A56), 0.4 ppm (T2, L3, F4, E5, L7, I28, W37, S52, L55, and A56), and/or 1.0 ppm (A6, I28, L55, and A56) for $^{15}N$, $^{1}H_N$, and/or $^{13}C_{methyl}$ nuclei, respectively, are colored according to residue type (green, hydrophobic; light blue, polar; and red, negatively charged). Note the reduced extent of the hydrophobic patch in the F state compared with the I state, accounting for the substantially reduced affinity of the F state for GroEL.

predominantly hydrophobic in nature because substitution of deuterium in nonexchangeable hydrogen positions decreases the strength of nonpolar sidechain interactions (22), the concomitant decrease in $k_{FI}^{G}$ and some reduction in $k_{IF}^{G}$ are manifestations of secondary deuterium kinetic isotope effects (23) on the catalytic activity of GroEL, presumably as a result of a destabilization of the transition state for the F-G to I-G exchange reaction in deuterated vs. protonated $SH3^{Mut}$.

**Chemical Shift Perturbation Mapping from Relaxation Dispersion.** CPMG relaxation dispersion data also contain information on the chemical shifts ($\varpi$) of exchanging species. Very close agreement is obtained between the absolute differences in chemical shifts between the unbound I and F states, $|\Delta\varpi^{F,I}|$, extracted from the global fits in this work and those reported earlier (15) for all probes (Fig. S2 *A–C*), as well as between the $^{15}N$ $|\Delta\varpi^{F,I}|$ values derived from the $^{15}N$/protonated and [$^{15}N$/$^{1}H_N$/ AILV-$^{13}CH_3$]/deuterated samples of $SH3^{Mut}$ (Fig. S2*D*). Extraction of the differences in chemical shifts between the I-G and I states, $\Delta\varpi^{I,I\text{-}G}$, which report on the location of the binding surface on $SH3^{Mut}$, is more problematic for the set of populations and rate constants pertinent to the present study (Fig. 3 and Table 2). Adopting a semiquantitative approach as described in *SI Theory* and illustrated in Fig. S9, we were able to obtain conservative estimates of a subset of $^{15}N$, $^{1}H_N$, and $^{13}C_{methyl}$ $\Delta\varpi^{I,I\text{-}G}$ values for $SH3^{Mut}$. This allowed us to approximately map the GroEL binding site on the surface of the protein as shown in Fig. 4*B*, where only those residues with values of $|\Delta\varpi^{I,I\text{-}G}| > 1.0$ ppm for $^{15}N$, 0.4 ppm for $^{1}H_N$, and/or 1.0 ppm for $^{13}C_{methyl}$ nuclei are highlighted. Whereas the $\Delta\varpi^{I,I\text{-}G}$ values provide no evidence for any further unfolding of the I state upon binding GroEL, significant chemical shift perturbations between the I and I-G states are observed for residues located in the N (Thr2, Leu3, Phe4, Glu5, Ala6, Leu7)- and C (Ile50, Ser52, Leu55, Ala56)-terminal regions, as well as for Ile28 ($^{13}C\delta_1$) and Trp37 ($^{1}H_N$) in strands β5 and β6, respectively. These residues form a contiguous hydrophobic patch that is exposed on the surface of the I state of $SH3^{Mut}$ (Fig. 4*B*, *Left*), but is much less prominent in the folded state where Phe4 and Ile28 are buried and Leu3 is partially occluded by Asp59 (Fig. 4*B*, *Right*).

**Concluding Remarks.** Using a series of multinuclear relaxation-based NMR techniques to probe invisible dark states of substrates bound to a megadalton macromolecular machine at occupancies below 1% that are inaccessible to conventional structural and biophysical techniques (16), we have been able to directly demonstrate that apo GroEL has intrinsic unfoldase/foldase activity on a nonaggregating, well-characterized (both kinetically and structurally) metastable substrate protein ($SH3^{Mut}$). Stabilization of the transition state for interconversion between folded and intermediate states of $SH3^{Mut}$ bound to GroEL is largely achieved through enhanced hydrophobic interactions of the intermediate state with the walls of the GroEL chambers. Previous investigations had

**Table 2. Summary of association, dissociation, and interconversion rate constants and species populations at 10 °C describing the interaction of $SH3^{Mut}$ with GroEL**

| Parameters | $^{15}N$/protonated | [$^{15}N$/$^{1}H_N$/AILV-$^{13}CH_3$]/deuterated |
|---|---|---|
| $k_{on}^{app}$, $s^{-1}$* | 60 ± 20 | 60 ± 20 |
| $k_{off}$, $s^{-1}$ | 200 ± 60 | 400 ± 100 |
| $k'_{off}$, $s^{-1}$ | 2.5(±1.0)×$10^4$ | 2.4(±1.0)×$10^4$ |
| $k_{FI}$, $s^{-1}$ | 7.5 ± 0.1† | 9.0 ± 0.2 |
| $k_{IF}$, $s^{-1}$ | 310 ± 20† | 350 ± 20 |
| $k_{FI}^{G}$, $s^{-1}$ | 4000 ± 2000‡ | 1200 ± 500‡ |
| $k_{IF}^{G}$, $s^{-1}$ | 1300 ± 500‡ | 800 ± 300‡ |
| $p_I$, % | 2.3 ± 0.2 | 2.5 ± 0.2 |
| $p_{I-G}$, % | 0.7 ± 0.2‡ | 0.4 ± 0.2‡ |
| $p_{F-G}$, % | 0.25 ± 0.15‡ | 0.30 ± 0.15‡ |

The kinetic scheme for the interaction of $SH3^{Mut}$ with GroEL is shown in Fig. 3. The range of parameters reported for [$^{15}N$/$^{1}H_N$/AILV-$^{13}CH_3$]/deuterated-$SH3^{Mut}$ covers the variation observed between ($^{15}N$, $^{1}H_N$) and $^{13}C_{methyl}$ probes (details of both sets of fits in *SI Theory*). Note that the values of the rate constants have been appropriately rounded and hence do not exactly satisfy the principle of detailed balance (compare *SI Theory*, Eq. **S2**); however, exact detailed balance is maintained in the global fitting procedure where the value of $k_{IF}^{G}$ is calculated directly from the values of the other rate constants.

*Assuming one binding site per GroEL cavity at a concentration of 17 μM (120 μM per GroEL subunit), the pseudo-first-order rate constant $k_{on}^{app}$ translates into a second-order association rate constant of ~3.5 × $10^6$ $M^{-1}{\cdot}s^{-1}$.

†The values of $k_{FI}$ and $k_{IF}$ determined by Neudecker et al. (14) at the same temperature are 7.1 ± 0.1 $s^{-1}$ and 258 ± 11 $s^{-1}$ for a $^{15}N$/protonated sample.

‡The reported error encompasses the variation observed in multiple fits using different starting conditions and weighting factors (details in *SI Theory*).

**Table 3. Average fitted values of $^{15}N$- and $^{1}H_N$-$R_2^{bound}$ values obtained for $^{15}N$/protonated-SH3 and [$^{15}N$/$^{1}H_N$/AILV-$^{13}CH_3$]/deuterated-SH3 in complex with GroEL**

| Labeling scheme nucleus, field | $R_2^{bound}$, $s^{-1}$ | |
|---|---|---|
| | $SH3^{Mut}$ | $SH3^{WT}$ |
| $^{15}N$/protonated-SH3 | | |
| $^{15}N$, 900 MHz | 889 ± 192 | 913 ± 158 |
| $^{15}N$, 600 MHz | 627 ± 124 | 669 ± 132 |
| [$^{15}N$/$^{1}H_N$/AILV-$^{13}CH_3$]/deuterated-SH3 | | |
| $^{15}N$, 900 MHz | 760 ± 158 | 730 ± 126 |
| $^{15}N$, 600 MHz | 610 ± 110 | 600 ± 99 |
| $^{1}H_N$, 800 MHz | 880 ± 199 | * |
| $^{1}H_N$, 600 MHz | 810 ± 192 | * |

All data are reported as the mean ± SD of the obtained distributions of values. Data for residues 1, 2 and 59, 60 at the N and C termini, respectively, are excluded as these retain considerable mobility in the bound state.

*The I-G and F-G states were assumed to have the same $^{1}H_N$-$R_2^{bound}$ values.

suggested that GroEL may possess intrinsic unfoldase activity but the conclusions were drawn from indirect evidence and/or involved poorly defined, heterogeneous systems (12, 13). The intrinsic unfoldase activity of apo GroEL presented here is distinct from the encapsulation cycle and supports the proposed iterative annealing mechanism of GroEL activity (24, 25), whereby an incorrectly folded, kinetically trapped substrate is unfolded on the internal surface of GroEL and subsequently released either into the GroEL cavity or into free solution where further attempts at correct folding can occur.

We previously showed that the interaction of a model intrinsically disordered peptide (amyloid β) with GroEL occurred through two contiguous hydrophobic patches [that is, a run of 3–5 hydrophobic residues separated from one another by at least 22 residues (26)] that can span adjacent GroEL subunits (20), thereby enabling the movement of GroEL subunits in response to ATP binding to exert force on the protein substrate (27, 28). In the case of Fyn SH3, the single hydrophobic patch exposed on the surface of the I state (Fig. 4*B*) is constituted by noncontiguous residues and can interact only with a single GroEL binding site; hence acceleration of the interconversion between the F and I states when bound to GroEL would not be expected to be further enhanced by ATP-induced domain reorientations. Further, although identification of contiguous hydrophobic residues is a simple bioinformatics exercise (26), identification of noncontiguous residues that could potentially form a surface-exposed hydrophobic patch on a misfolded or partially folded protein would be impossible to predict in the absence of structural knowledge of such states. The ability of GroEL to recognize both contiguous and noncontiguous hydrophobic patches adds an additional layer of complexity to the GroEL-substrate recognition problem, but it seems entirely plausible that larger protein substrates, depending on their conformational state, might use a mixture of both modalities.

The rigid body domain movements that accompany the binding of GroES to GroEL and the binding and hydrolysis of ATP (29) probably function to further enhance the intrinsic unfoldase activity of GroEL in cases where the substrate can contact two or more GroEL subunits simultaneously, by allowing GroEL to perform mechanical (i.e., active) work (28) whereby the bound protein substrate can be partially stretched apart (27). From an evolutionary perspective one might speculate that the simple unfoldase activity evolved first, and the complex, ATP-driven unfolding and encapsulation mechanism followed later. This hypothesis is supported by the observation that a minichaperone comprising only a single apical domain of GroEL can facilitate protein folding both in vitro and in vivo (30). Additionally, the demonstrated intrinsic unfoldase activity of apo GroEL provides an explanation of how GroEL reduces the rate at which protein fibrils are formed in vitro (2).

In conclusion, these observations provide a basis for understanding how GroEL and by extension related chaperonins assist protein folding and demonstrate that chaperonins have evolved both passive (i.e., intrinsic unfoldase/foldase activity in the apo state) and active (i.e., ATP-driven) mechanisms for protecting the cell from the deleterious effects of protein misfolding.

## Materials and Methods

SH3 samples (both wild type and triple mutant) were isotopically labeled either with $^{15}N$ or with $^{15}N$, $^{2}H$ (except $^{1}H_N$ protons, which are protonated through exchange with water) and selective $^{13}C_{methyl}$ labeling of Ala-β, Ile-δ1, Leu-δ, and Val-γ methyl groups (full details in *SI Materials and Methods*). Purification and expression of the SH3 domains, GroEL and Rubisco were carried out as described in *SI Materials and Methods*. The majority of NMR samples contained 100 μM SH3 and 120 μM (in subunits) GroEL in 50 mM sodium phosphate, pH 7.0, 0.2 mM EDTA, 0.05% (wt/vol) $NaN_3$, 10% (vol/vol) $D_2O$. All NMR experiments were conducted at 10 °C on NMR spectrometers operating at $^{1}H$ frequencies of 900 MHz, 800 MHz, 600 MHz, and 500 MHz and equipped with triple-resonance z-gradient cryoprobes. Details of the $^{15}N$-, $^{1}H$-, and $^{13}C_{methyl}$-CPMG; $^{15}N$- and $^{13}C_{methyl}$-$\Delta R_2$; and $^{15}N$- and $^{13}C_{methyl}$-DEST experiments are provided in *SI Materials and Methods*. Simultaneous fitting of the experimental data to the relevant kinetic schemes using the McConnell equations (31) was performed in Matlab as described in *SI Theory*.

**ACKNOWLEDGMENTS.** We thank G. H. Lorimer and A. Szabo for insightful discussions, G. H. Lorimer for the GroEL and Rubisco clones, and L. E. Kay for the original Fyn SH3 clones. This work was supported by the intramural program of the National Institute of Diabetes and Digestive and Kidney Diseases/National Institutes of Health (NIDDK/NIH) and the AIDS Targeted Antiviral Program of the NIH Director (G.M.C.).

1. Dobson CM (2003) Protein folding and misfolding. *Nature* 426(6968):884–890.
2. Hartl FU, Bracher A, Hayer-Hartl M (2011) Molecular chaperones in protein folding and proteostasis. *Nature* 475(7356):324–332.
3. Thirumalai D, Lorimer GH (2001) Chaperonin-mediated protein folding. *Ann Rev Biophys Biomol Struct* 30:245–269.
4. Spiess C, Meyer AS, Reissmann S, Frydman J (2004) Mechanism of the eukaryotic chaperonin: Protein folding in the chamber of secrets. *Trends Cell Biol* 14(11):598–604.
5. Saibil HR (2008) Chaperone machines in action. *Curr Opin Struct Biol* 18(1):35–42.
6. Horwich AL, Fenton WA (2009) Chaperonin-mediated protein folding: Using a central cavity to kinetically assist polypeptide chain folding. *Q Rev Biophys* 42(2):83–116.
7. Lin Z, Rye HS (2006) GroEL-mediated protein folding: Making the impossible, possible. *Crit Rev Biochem Mol Biol* 41(4):211–239.
8. Farr GW, et al. (2003) Folding with and without encapsulation by cis- and trans-only GroEL-GroES complexes. *EMBO J* 22(13):3220–3230.
9. Robinson CV, et al. (1994) Conformation of GroEL-bound α-lactalbumin probed by mass spectrometry. *Nature* 372(6507):646–651.
10. Zahn R, Spitzfaden C, Ottiger M, Wüthrich K, Plückthun A (1994) Destabilization of the complete protein secondary structure on binding to the chaperone GroEL. *Nature* 368(6468):261–265.
11. Zahn R, Perrett S, Stenberg G, Fersht AR (1996) Catalysis of amide proton exchange by the molecular chaperones GroEL and SecB. *Science* 271(5249):642–645.
12. Zahn R, Perrett S, Fersht AR (1996) Conformational states bound by the molecular chaperones GroEL and secB: A hidden unfolding (annealing) activity. *J Mol Biol* 261(1):43–61.
13. Priya S, et al. (2013) GroEL and CCT are catalytic unfoldases mediating out-of-cage polypeptide refolding without ATP. *Proc Natl Acad Sci USA* 110(18):7199–7204.
14. Neudecker P, et al. (2006) Identification of a collapsed intermediate with non-native long-range interactions on the folding pathway of a pair of Fyn SH3 domain mutants by NMR relaxation dispersion spectroscopy. *J Mol Biol* 363(5):958–976.
15. Neudecker P, et al. (2012) Structure of an intermediate state in protein folding and aggregation. *Science* 336(6079):362–366.
16. Anthis NJ, Clore GM (2015) Visualizing transient dark states by NMR spectroscopy. *Q Rev Biophys* 48(1):35–116.
17. Fawzi NL, Ying J, Torchia DA, Clore GM (2010) Kinetics of amyloid β monomer-to-oligomer exchange by NMR relaxation. *J Am Chem Soc* 132(29):9948–9951.
18. Fawzi NL, Ying J, Ghirlando R, Torchia DA, Clore GM (2011) Atomic-resolution dynamics on the surface of amyloid-β protofibrils probed by solution NMR. *Nature* 480(7376):268–272.
19. Palmer AG, 3rd (2014) Chemical exchange in biomacromolecules: Past, present, and future. *J Magn Reson* 241:3–17.
20. Libich DS, Fawzi NL, Ying J, Clore GM (2013) Probing the transient dark state of substrate binding to GroEL by relaxation-based solution NMR. *Proc Natl Acad Sci USA* 110(28):11361–11366.
21. van der Vies SM, Viitanen PV, Gatenby AA, Lorimer GH, Jaenicke R (1992) Conformational states of ribulosebisphosphate carboxylase and their interaction with chaperonin 60. *Biochemistry* 31(14):3635–3644.
22. Hattori A, Crespi HL, Katz JJ (1965) Effect of side-chain deuteration on protein stability. *Biochemistry* 4(7):1213–1225.
23. Dahlquist FW, Rand-Meir T, Raftery MA (1969) Application of secondary alpha-deuterium kinetic isotope effects to studies of enzyme catalysis. Glycoside hydrolysis by lysozyme and beta-glucosidase. *Biochemistry* 8(10):4214–4221.
24. Corrales FJ, Fersht AR (1995) The folding of GroEL-bound barnase as a model for chaperonin-mediated protein folding. *Proc Natl Acad Sci USA* 92(12):5326–5330.
25. Todd MJ, Lorimer GH, Thirumalai D (1996) Chaperonin-facilitated protein folding: Optimization of rate and yield by an iterative annealing mechanism. *Proc Natl Acad Sci USA* 93(9):4030–4035.
26. Stan G, Brooks BR, Lorimer GH, Thirumalai D (2006) Residues in substrate proteins that interact with GroEL in the capture process are buried in the native state. *Proc Natl Acad Sci USA* 103(12):4433–4438.
27. Lin Z, Madan D, Rye HS (2008) GroEL stimulates protein folding through forced unfolding. *Nat Struct Mol Biol* 15(3):303–311.
28. Corsepius NC, Lorimer GH (2013) Measuring how much work the chaperone GroEL can do. *Proc Natl Acad Sci USA* 110(27):E2451–E2459.
29. Sharma S, et al. (2008) Monitoring protein conformation along the pathway of chaperonin-assisted folding. *Cell* 133(1):142–153.
30. Chatellier J, Hill F, Lund PA, Fersht AR (1998) In vivo activities of GroEL mini-chaperones. *Proc Natl Acad Sci USA* 95(17):9861–9866.
31. McConnell HM (1958) Reaction rates by nuclear magnetic resonance. *J Chem Phys* 28(3):430–431.
32. Braig K, et al. (1994) The crystal structure of the bacterial chaperonin GroEL at 2.8 A. *Nature* 371(6498):578–586.
33. Cavanagh J, Fairbrother WJ, Palmer AG, Rance M, Skelton NJ (2007) *Protein NMR Spectroscopy: Principles and Practice* (Elsevier Academic Press, San Diego), 2nd Ed.
34. Helgstrand M, Härd T, Allard P (2000) Simulations of NMR pulse sequences during equilibrium and non-equilibrium chemical exchange. *J Biomol NMR* 18(1):49–63.
35. Fawzi NL, Ying J, Torchia DA, Clore GM (2012) Probing exchange kinetics and atomic resolution dynamics in high-molecular-weight complexes using dark-state exchange saturation transfer NMR spectroscopy. *Nat Protoc* 7(8):1523–1533.
36. Kapust RB, et al. (2001) Tobacco etch virus protease: Mechanism of autolysis and rational design of stable mutants with wild-type catalytic proficiency. *Protein Eng* 14(12):993–1000.
37. Maxwell KL, Davidson AR (1998) Mutagenesis of a buried polar interaction in an SH3 domain: Sequence conservation provides the best prediction of stability effects. *Biochemistry* 37(46):16172–16182.
38. Tugarinov V, Kanelis V, Kay LE (2006) Isotope labeling strategies for the study of high-molecular-weight proteins by solution NMR spectroscopy. *Nat Protoc* 1(2):749–754.
39. Tugarinov V, Kay LE (2004) An isotope labeling strategy for methyl TROSY spectroscopy. *J Biomol NMR* 28(2):165–172.
40. Grason JP, Gresham JS, Lorimer GH (2008) Setting the chaperonin timer: A two-stroke, two-speed, protein machine. *Proc Natl Acad Sci USA* 105(45):17339–17344.
41. Lakomek NA, Ying J, Bax A (2012) Measurement of $^{15}$N relaxation rates in perdeuterated proteins by TROSY-based methods. *J Biomol NMR* 53(3):209–221.
42. Kay LE, et al. (1992) The measurement of heteronuclear transverse relaxation-times in Ax3 spin systems via polarization-transfer techniques. *J Magn Reson* 100(3):538–558.
43. Bouvignies G, Kay LE (2012) A 2D $^{13}$C-CEST experiment for studying slowly exchanging protein systems using methyl probes: An application to protein folding. *J Biomol NMR* 53(4):303–310.
44. Kay LE, Torchia DA (1991) The effects of dipolar cross-correlation on $^{13}$C methyl-carbon T1, T2, and NOE measurements in macromolecules. *J Magn Reson* 95(3):536–547.
45. Fawzi NL, Libich DS, Ying J, Tugarinov V, Clore GM (2014) Characterizing methyl-bearing side chain contacts and dynamics mediating amyloid β protofibril interactions using $^{13}$C(methyl)-DEST and lifetime line broadening. *Angew Chem Int Ed Engl* 53(39):10345–10349.
46. Delaglio F, et al. (1995) NMRPipe: A multidimensional spectral processing system based on UNIX pipes. *J Biomol NMR* 6(3):277–293.
47. Meiboom S, Gill D (1958) Modified spin-echo method for measuring nuclear relaxation times. *Rev Sci Instrum* 29(8):688–691.
48. Hansen DF, Vallurupalli P, Kay LE (2008) An improved $^{15}$N relaxation dispersion experiment for the measurement of millisecond time-scale dynamics in proteins. *J Phys Chem B* 112(19):5898–5904.
49. Ishima R, Torchia DA (2003) Extending the range of amide proton relaxation dispersion experiments in proteins using a constant-time relaxation-compensated CPMG approach. *J Biomol NMR* 25(3):243–248.
50. Korzhnev DM, Neudecker P, Mittermaier A, Orekhov VY, Kay LE (2005) Multiple-site exchange in proteins studied with a suite of six NMR relaxation dispersion experiments: An application to the folding of a Fyn SH3 domain mutant. *J Am Chem Soc* 127(44):15602–15611.
51. Lundström P, Vallurupalli P, Religa TL, Dahlquist FW, Kay LE (2007) A single-quantum methyl 13C-relaxation dispersion experiment with improved sensitivity. *J Biomol NMR* 38(1):79–88.
52. Augustyniak R, Ferrage F, Paquin R, Lequin O, Bodenhausen G (2011) Methods to determine slow diffusion coefficients of biomolecules: Applications to Engrailed 2, a partially disordered protein. *J Biomol NMR* 50(3):209–218.
53. Choy WY, et al. (2002) Distribution of molecular size within an unfolded state ensemble using small-angle X-ray scattering and pulse field gradient NMR techniques. *J Mol Biol* 316(1):101–112.

# Supporting Information

## Libich et al. 10.1073/pnas.1510083112

### SI Theory

At 10 °C $SH3^{Mut}$ undergoes slow exchange between the major folded (**F**) state and a sparsely populated folding intermediate (**I**) (14, 15). The population of the unfolded state (**U**) is negligibly small under these conditions, beyond the limits of detection by Carr–Purcell–Meinboom–Gill (CPMG) relaxation dispersion, and can therefore be safely ignored (14). Both states **F** and **I** bind to GroEL, with the affinity of the former being several orders of magnitude weaker ($K_{diss}$ in the millimolar range) than the latter ($K_{diss} \sim 60$ μM). The interconversion between the free and GroEL-bound states of **F** and **I** can described by a four-state kinetic scheme (Fig. 3 of main text),

$$\begin{array}{ccc} \mathbf{F} & \underset{k_{IF}}{\overset{k_{FI}}{\rightleftharpoons}} & \mathbf{I} \\ k'_{off} \uparrow\downarrow k_{on}^{app} & & k_{off} \uparrow\downarrow k_{on}^{app} \\ \mathbf{F\text{-}G} & \underset{k_{IF}^{G}}{\overset{k_{FI}^{G}}{\rightleftharpoons}} & \mathbf{I\text{-}G} \end{array}, \qquad [S1]$$

where **F-G** and **I-G** represent the complexes of **F** and **I** with GroEL. In the kinetic scheme (Eq. **S1**), the following relationship must hold:

$$k_{FI} k_{on}^{app} k_{IF}^{G} k'_{off} = k_{on}^{app} k_{FI}^{G} k_{off} k_{IF}. \qquad [S2]$$

The complexity of the four-state system described by Eq. **S1** precludes detailed characterization without a few simplifying assumptions. Specifically, we assume that (*i*) the apparent pseudo-first-order association rate constants for the binding of **F** and **I** ($k_{on}^{app}$) to GroEL are diffusion controlled and therefore the same (since both states have the same charge, and further the charge of $SH3^{WT}$ and $SH3^{Mut}$ are identical), and (*ii*) GroEL binding of the mutant state **F** is the same as that of the wild type and can therefore be described by measurements of NMR parameters on $SH3^{WT}$ in the absence and presence of GroEL. These assumptions and the fact that the kinetics of interconversion between states **F** and **I** ($k_{FI}$ and $k_{IF}$) can be characterized separately via CPMG experiments in the absence of GroEL allow us to "dissect" this complex set of equilibria onto simpler components that can be analyzed separately.

All of the experimental data [$\Delta R_2$, CPMG, and dark state exchange saturation transfer (DEST)] for $^{15}N$ in the case of $^{15}N$/protonated-SH3 and for methyl groups in the case of [$^{15}N$/$^{1}H_N$/AILV-$^{13}CH_3$]/deuterated-SH3 were fitted simultaneously by minimizing the following sum of squared differences, *F*, between the observed and calculated values of the experimental observables, using an in-house Matlab program,

$$\begin{aligned} F = {} & \alpha_1 \sum_i \sum_{j=1}^{2} \left( \frac{\Delta R_{2,WT+GroEL}^{obs,i,j} - \Delta R_{2,WT+GroEL}^{calc,2-state,i,j}}{\sigma_{\Delta R_{2,WT}^{obs,i,j}}} \right)^2 \\ & + \alpha_2 \sum_i \sum_{j=1}^{2} \left( \frac{\Delta R_{2,Mut+GroEL}^{obs,i,j} - \Delta R_{2,Mut+GroEL}^{calc,i,j}}{\sigma_{\Delta R_{2,WT}^{obs,i,j}}} \right)^2 \\ & + \alpha_3 \sum_i \sum_k \sum_{j=1}^{2} \left( \frac{\Delta R_{2,Mut\ free}^{obs,i,k,j} - R_{2,Mut\ free}^{calc,2-state,i,k,j}}{\sigma_{R_{2,Mut\ free}^{obs,i,k,j}}} \right)^2 \\ & + \alpha_4 \sum_i \sum_k \sum_{j=1}^{2} \left( \frac{R_{2,Mut+GroEL}^{obs,i,k,j} - R_{2,Mut+GroEL}^{calc,i,k,j}}{\sigma_{R_{2,Mut+GroEL}^{obs,i,k,j}}} \right)^2 \\ & + \alpha_5 \sum_i \sum_{l=1} \sum_{m=1}^{2} \left( \kappa_{Mut+GroEL}^{obs,i,l,m} - \kappa_{Mut+GroEL}^{calc,i,l,m} \right)^2, \end{aligned} \qquad [S3]$$

where the first and second terms relate to the differences in $R_2$ values measured for the wild type and mutant, respectively, in the presence and absence of GroEL; the third and fourth terms to CPMG data on the mutant in the absence and presence of GroEL, respectively; and the fifth term to DEST experiments on the mutant in the presence of GroEL. (Note that no CPMG dispersions were observed for the wild type in the presence of GroEL, and the DEST profiles for the wild type in the absence and presence of GroEL were essentially the same within experimental error.) The subscripts *i*, *j*, *k*, *l*, and *m* in Eq. **S3** refer to residue number, $^{1}H$ spectrometer frequency (600 MHz and 900 MHz for $^{15}N$ and 600 MHz and 800 MHz for $^{13}C_{methyl}$ data), CPMG field, DEST offset, and DEST field strength (500 Hz and 750 Hz for $^{15}N$, and 750 Hz and 1500 Hz for $^{13}C_{methyl}$), respectively; and $\alpha_1$, $\alpha_2$, $\alpha_3$, $\alpha_4$, and $\alpha_5$ represent empirically determined factors used to appropriately weight the different data types and have numerical values of 1, 0.5, 3, 1, and 1, respectively. For analysis of the data collected on [$^{15}N$/$^{1}H_N$/AILV-$^{13}CH_3$]/deuterated-SH3 samples, the error function *F′* in Eq. **S4** was extended to include $^{1}H_N$ CPMG relaxation dispersion data for the free $SH3^{Mut}$ and $SH3^{Mut}$ + GroEL,

$$\begin{aligned} F' = {} & F + \alpha_6 \sum_i \sum_k \sum_{j=1}^{2} \left( \frac{R_{2,Mut\ free}^{obs,i,j,k} - R_{2,Mut\ free}^{calc,2-state,i,k,j}}{\sigma_{R_{2,Mut\ free}^{obs,i,k,j}}} \right)^2 \\ & + \alpha_7 \sum_i \sum_k \sum_{j=1}^{2} \left( \frac{R_{2,Mut+GroEL}^{obs,i,k,j} - R_{2,Mut+GroEL}^{calc,i,k,j}}{\sigma_{R_{2,Mut+GroEL}^{obs,i,k,j}}} \right)^2, \end{aligned} \qquad [S4]$$

where *F* is defined in Eq. **S3** and the factors $\alpha_6$ and $\alpha_7$ have numerical values of 0.5 and 3, respectively.

The values of $\Delta R_2$ for $SH3^{WT}$ ($\Delta R_{2,WT}$), obtained from the difference in $R_2$ values measured in the presence and absence of GroEL (the first term of Eq. **S3**), are used to characterize the binding of state **F** to GroEL via a two-state fit (providing $k_{on}^{app}$ and $k'_{off}$), whereas the CPMG data obtained on $SH3^{Mut}$ in the absence of GroEL ($R_{2,Mut\ free}$, the third term in Eq. **S3**) are used to characterize the transition **F**↔**I** via a two-state fit providing $k_{FI}$ and $k_{IF}$. The space of residue-specific fitted parameters for analysis of the [U-$^{15}N$]-SH3 data included $R_{2,I\text{-}G/F\text{-}G}^{900}$, $R_{2,I\text{-}G/F\text{-}G}^{600}$, $R_{2,WT+GroEL}^{900}$, $R_{2,WT+GroEL}^{600}$, $R_{2,F/I}^{900}$, $R_{2,F/I}^{600}$, $\Delta\varpi^{I,I\text{-}G}$, and $\Delta\varpi^{F,I}$, where $R_{2,n}$ denotes the $R_2$ of state (sample) *n* and the superscripts denote spectrometer fields; $\Delta\varpi^{m,n}$ are the differences in chemical shifts between states *n* and *m* ($\Delta\varpi^{n} - \Delta\varpi^{m}$); and for analysis of the $SH3^{Mut}$ data, this set of parameters was extended to include $^{1}H_N$ relaxation rates in the bound (**F-G** and **I-G**) states (denoted with the superscript "HN") and the changes in the chemical shifts of $^{1}H_N$ nuclei, $\Delta\varpi^{HN;m,n}$: $R_{2,I\text{-}G/F\text{-}G}^{900}$, $R_{2,I\text{-}G/F\text{-}G}^{600}$, $R_{2,WT+GroEL}^{900}$, $R_{2,WT+GroEL}^{600}$, $R_{2,F/I}^{900}$, $R_{2,F/I}^{600}$, $\Delta\varpi^{I,I\text{-}G}$, $\Delta\varpi^{F,I}$, $R_{2,I\text{-}G/F\text{-}G}^{HN,900}$, $R_{2,I\text{-}G/F\text{-}G}^{HN,600}$, $\Delta\varpi^{HN;\ I,I\text{-}G}$, and $\Delta\varpi^{HN;\ F,I}$. In the fits of the [$^{15}N$/$^{1}H_N$/AILV-$^{13}CH_3$]/deuterated-$SH3^{Mut}$ data, the values of $^{15}N$ $\Delta\varpi^{I,I\text{-}G}$ were constrained to within ±2.5 SD from the mean $\Delta\varpi^{I,I\text{-}G}$ values obtained from the $^{15}N$/protonated $SH3^{Mut}$ data. This latter constraint is entirely reasonable because deuteration has no effect on $^{15}N$ $\Delta\varpi^{F,I}$ (Fig. S2*D*) and hence can be assumed to have no substantial effect on the differences in $^{15}N$ chemical shifts between

other species. To account for large differences between $^{13}C_{methyl}$ $R_2$ rates and methyl single-quantum (SQ) relaxation rates effective in CPMG experiments (a ratio $R_{2,CPMG}/R_2$ of 1.6 on average was observed in the samples of free SH3$^{mut}$), the SQ $^{13}C_{methyl}$ relaxation rates (denoted with the superscript "CPMG") of the bound states were separated from those corresponding to $^{13}C_{methyl}$ $R_2$ rates in the $\Delta R_2$ and DEST experiments, resulting in the following extended set of fitted parameters used for analysis of $^{13}C_{methyl}$ data: $R_{2,\text{I-G/F-G}}^{C,800}$, $R_{2,\text{I-G/F-G}}^{C,600}$, $R_{2,\text{I-G/F-G}}^{CPMG,800}$, $R_{2,\text{I-G/F-G}}^{CPMG,600}$, $R_{2,\text{WT+GroEL}}^{C,800}$, $R_{2,\text{WT+GroEL}}^{C,600}$, $R_{2,\text{F/I}}^{C,800}$, $R_{2,\text{F/I}}^{C,600}$, $\Delta\varpi^{C;\,\text{I,I-G}}$, and $\Delta\varpi^{C;\,\text{F,I}}$.

The $R_2$ values of the GroEL-bound states (**F-G** and **I-G**) were assumed to be the same, as well as the $R_2$ values of states **F** and **I**. The set of six global fitted parameters included $p_{\text{I-G}}$, $k_{on}^{app}$, $k'_{off}$, $k_{FI}^{G}$, $k_{FI}$, and $k_{IF}$, where $p_n$ is the population of state $n$, and the rate constants are defined in Eq. **S2**. Note that the residue-specific $R_2$ values in the bound states, $R_{2,\text{I-G/F-G}}^{900}$ and $R_{2,\text{I-G/F-G}}^{600}$, $\Delta\varpi^{\text{F,I}}$ and the rate constants $(k_{FI}, k_{IF})$, $(k_{on}^{app}, k'_{off})$, are "shared" between different types of data and fitting models in the course of the minimization procedure: Namely, the $\Delta R_{2,WT}$ data (the first term in Eq. **S3**) for SH3$^{WT}$ and the CPMG data for free SH3$^{Mut}$ (the third term in Eq. **S3**) are fitted using a two-state model, whereas the rest of the data (SH3$^{Mut}$ + GroEL) are modeled using the full four-state model.

The set of parameters derived a posteriori from the fitted global parameters was calculated as follows. First, the population of state **I**, $p_I$, can be calculated from the relationship

$$p_I = \frac{(1-p_{\text{I-G}})}{\left[1+(k_{IF}/k_{FI})\left(1+k_{on}^{app}/k'_{off}\right)\right]} \qquad \textbf{[S5]}$$

from which it follows that $p_F = p_1 k_{IF}/k_{FI}$, and $p_{\text{F-G}} = 1 - p_{\text{I-G}} - p_F - p_I$. The derived rate constants are then given by $k_{off} = k_{on}^{app} p_I/p_{\text{I-G}}$ and $k_{IF}^{G} = k_{FI}^{G} k_{IF} k_{off}/k_{FI} k'_{off} = k_{FI}^{G} p_{\text{F-G}}/p_{\text{I-G}}$.

The uncertainties in the values of the optimized parameters, corresponding to confidence intervals of ±1 SD, were determined from the variance–covariance matrix of the nonlinear fit. Convergence of the solution was confirmed by varying initial values for all parameters and obtaining the same solution within reported uncertainties.

Below, we describe how each of the data types (CPMG, DEST, and $\Delta R_2$) used in the calculation of the error function $F$ in Eqs. **S3** and **S4** is modeled for comparison with the observed experimental values.

The evolution of magnetization during the CPMG constant time period for the system in Eq. **S1** can be represented by

$$M(t) = (AA^*A^*A)^n M(0), \qquad \textbf{[S6]}$$

where $M = [M^{\text{F}}; M^{\text{I}}; M^{\text{F-G}}; M^{\text{I-G}}]^T$; $M^n$ denotes the transverse magnetization of state $n$; $T$ denotes transposition; $A = \exp(-R\tau_{CP}/2)$; $A^*$ is the complex conjugate of $A$; $n$ is the number of CPMG cycles used; $\tau_{CP}$ is the time interval between two consecutive 180° pulses in the CPMG pulse train; and $R = R^{cs} + R^{rel} + R^{ex}$, where

$$R^{cs} = i\begin{bmatrix} -\Delta\varpi^{\text{F,I}} & 0 & 0 & 0 \\ 0 & 0 & 0 & 0 \\ 0 & 0 & -\Delta\varpi^{\text{F-G,I}} & 0 \\ 0 & 0 & 0 & \Delta\varpi^{\text{I,I-G}} \end{bmatrix} \qquad \textbf{[S7]}$$

$$R^{rel} = \begin{bmatrix} R_2^{\text{F}} & 0 & 0 & 0 \\ 0 & R_2^{\text{I}} & 0 & 0 \\ 0 & 0 & R_2^{\text{F-G}} & 0 \\ 0 & 0 & 0 & R_2^{\text{I-G}} \end{bmatrix} \qquad \textbf{[S8]}$$

$$R^{ex} = \begin{bmatrix} k_{FI}+k_{on}^{app} & -k_{IF} & -k'_{off} & 0 \\ -k_{FI} & k_{IF}+k_{on}^{app} & 0 & -k_{off} \\ -k_{on}^{app} & 0 & k_{FI}^{G}+k'_{off} & -k_{IF}^{G} \\ 0 & -k_{on}^{app} & -k_{FI}^{G} & k_{FI}^{G}+k_{off} \end{bmatrix}, \qquad \textbf{[S9]}$$

where $\Delta\varpi^{m,n}$ is the difference between chemical shifts of states $n$ and $m$ ($\Delta\varpi^n - \Delta\varpi^m$), and $R_2^n$ is the transverse relaxation of state $n$ in the absence of exchange. Only states **F** and **I** were assumed to be present at the start of the CPMG train, $M(0) = (p_F, p_I, 0, 0)$, because essentially all magnetization in the sparsely populated **I-F** and **I-G** states will have decayed during the insensitive nuclei enhancement by polarization transfer (INEPT) before the CPMG pulse train owing to the very large $R_2$ values in the GroEL-bound states. The $R_2$ values for states **F** and **I** (assumed to be the same) were supplied for the calculation from the numerical two-state fits of the CPMG profiles obtained on the low-concentration (100 μM) sample of SH3$^{Mut}$ (see *SI Materials and Methods* on $^{15}N$ relaxation dispersion measurements). We note that these $R_2$ values are ∼40% lower on average than the fitted CPMG $R_2$ values obtained from measurements on the 10-fold more concentrated (1 mM) sample, but are only slightly lower (∼6% on average) than the $R_2$ values determined from $R_{1\rho}$ experiments on the same low-concentration (100 μM) sample due to off-resonance and radiofrequency field inhomogeneity effects inherent in CPMG experiments (33). The chemical shifts of the (bound) state **F-G** were assumed to be the same as those of state **F**; i.e., $\Delta\varpi^{\text{F,F-G}} = 0$ and hence $\Delta\varpi^{\text{F,I}} = \Delta\varpi^{\text{F-G,I}}$, a valid assumption because no relaxation dispersions were observed for SH3$^{WT}$ in the presence of GroEL, and thus our experimental data do not contain any information on $\Delta\varpi^{\text{F,F-G}}$. Relaxation dispersion profiles of the four-state equilibrium in Eq. **S1** were calculated using Eqs. **S6**–**S9** for the SH3$^{Mut}$+GroEL data (the fourth term in Eq. **S4**), whereas a numerical fit to a simple two-state (states **F** and **I** only) model was used for the GroEL-free (free SH3$^{Mut}$) data (the third term in Eq. **S3**).

Generally, in a three or more site exchanging system, the relative signs of the differences between the chemical shifts of the observable state, F, and one of the "dark" states, I or I-G ($\Delta\varpi^{\text{F,I}}$ and $\Delta\varpi^{\text{F,I-G}}$ defined as $\varpi^{\text{I}} - \varpi^{\text{F}}$ and $\varpi^{\text{I-G}} - \varpi^{\text{F}}$, respectively), can be obtained directly from the fits (14). Because the values and absolute signs of $\Delta\varpi^{\text{F,I}}$ (and therefore the values of $\varpi^{\text{I}}$) were determined previously for free SH3$^{Mut}$ at 20 °C (BioMagResBank entry no. 17149) (14, 15) and can be safely assumed to be temperature invariant (14), the values of $\Delta\varpi^{\text{I,I-G}}$ can, in principle, be obtained from: $\Delta\varpi^{\text{I,I-G}} = \Delta\varpi^{\text{F,I-G}} - \Delta\varpi^{\text{F,I}}$.

In practice, however, for the rate constants and populations pertinent to the present work (Fig. 3 and Table 2), the determination of $\Delta\varpi^{\text{I,I-G}}$ from the relationship above or from direct fitting is problematic. Fig. S9 shows simulated relaxation dispersion profiles for the four-state exchanging system of Fig. 3, using the rate constants and populations listed in Table 2 ($^{15}N$/protonated-SH3$^{Mut}$) for a set of $\Delta\varpi^{\text{F,I}}$ values. It is clear from these simulations that the profiles with the same absolute values of $\Delta\varpi^{\text{F,I-G}}$ but different signs (shown with circles and asterisks of the same color in Fig. S9) are, in general, barely distinguishable from one another, with the differences between them usually falling within the errors of the $R_{2,eff}$ measurements for the majority of residues in SH3$^{Mut}$. Because the signs of $\Delta\varpi^{\text{F,I-G}}$ cannot in most instances be differentiated in the fits of experimental data, the values of $\Delta\varpi^{\text{I,I-G}}$ can generally not be reliably determined. In fact, as far as the fitting of the experimental data is concerned, two solutions for $\Delta\varpi^{\text{I,I-G}}$ were obtained for most (but not all) residues of SH3$^{Mut}$—one corresponding to positive $\Delta\varpi^{\text{F,I-G}}$ and the other to negative $\Delta\varpi^{\text{F,I-G}}$—depending upon the starting conditions chosen for the minimization of the error function. For this reason and because the values of $\Delta\varpi^{\text{F,I}}$ and $\Delta\varpi^{\text{I,I-G}}$ are anticorrelated

(namely, a small positive change/error in $\Delta\varpi^{F,I}$ can lead to a large negative change in $\Delta\varpi^{I,I\text{-}G}$ and vice versa), we have adopted a semiquantitative approach toward the derivation of $\Delta\varpi^{I,I\text{-}G}$.

Estimation of $\Delta\varpi^{I,I\text{-}G}$ values was achieved by fitting individual (single-residue) relaxation dispersion profiles with all of the rate constants fixed to the values appropriate for each sample (Table 2) and starting from different initial conditions for the value of $\Delta\varpi^{I,I\text{-}G}$ (typically, $\Delta\varpi^{I,I\text{-}G} = 0$), whereas the $\Delta\varpi^{F,I}$ shifts were randomly varied within the SD of 10% of their mean values reported previously (14). The distributions of $\Delta\varpi^{I,I\text{-}G}$ obtained in this manner were carefully analyzed, and only the solutions that provided both realistic values of the chemical shifts of state I ($\varpi^{I}$) and realistic $R_2$ values of the bound (I-G) state were retained. Subsequently, the uncertainties in the fitted $|\Delta\varpi^{I,I\text{-}G}|$ were calculated from the root mean SD (rmsd) of the (retained) set of $|\Delta\varpi^{I,I\text{-}G}|$ values. The subset of residues that reproducibly provided lower bounds for $|\Delta\varpi^{I,I\text{-}G}|$ (the mean value minus the uncertainty) >1.0 ppm, 0.4 ppm, and/or 1.0 ppm for $^{15}$N, $^{1}$H$_N$, and/or $^{13}$C$_{methyl}$ nuclei, respectively, were used to map the GroEL binding site on SH3$^{Mut}$ (compare Fig. 4).

It is also noteworthy that the profiles with the smallest relaxation dispersion ($R_{ex}$) in Fig. S9 correspond to $\Delta\varpi^{F,I\text{-}G} = 0$ (black dotted curves), i.e., when the chemical shifts of the folded (F) and GroEL-bound intermediate (I-G) states are the same. In all cases, an increase in the absolute value of $\Delta\varpi^{F,I\text{-}G}$ leads to a larger relaxation dispersion (higher $R_{ex}$). This observation underscores the importance of estimating lower bounds for $|\Delta\varpi^{I,I\text{-}G}|$ rather than the values themselves, i.e., the bounds beyond which the contribution to exchange due to $\Delta\varpi^{I,I\text{-}G}$ is not supported by the experimental data.

The time-dependent magnetization in DEST and $\Delta R_2$ experiments for a single isolated spin in exchange between four different states (Eq. **S1**) can be represented by a set of McConnell equations (18, 31, 34, 35) as

$$\frac{d}{dt}\begin{bmatrix} E/2 \\ I_x^{F} \\ I_y^{F} \\ I_z^{F} \\ I_x^{I} \\ I_y^{I} \\ I_z^{I} \\ I_x^{F\text{-}G} \\ I_y^{F\text{-}G} \\ I_z^{F\text{-}G} \\ I_x^{I\text{-}G} \\ I_y^{I\text{-}G} \\ I_z^{I\text{-}G} \end{bmatrix} = -\begin{bmatrix} 0 & 0 & 0 & 0 & 0 & 0 & 0 & 0 & 0 & 0 & 0 & 0 & 0 \\ 0 & R_2^{F^*} & \Omega^{F} & -\omega_y & -k_{IF} & 0 & 0 & -k'_{off} & 0 & 0 & 0 & 0 & 0 \\ 0 & -\Omega^{F} & R_2^{F^*} & \omega_x & 0 & -k_{IF} & 0 & 0 & -k'_{off} & 0 & 0 & 0 & 0 \\ -2\Theta^{F} & \omega_y & -\omega_x & R_1^{F^*} & 0 & 0 & -k_{IF} & 0 & 0 & -k'_{off} & 0 & 0 & 0 \\ 0 & -k_{FI} & 0 & 0 & R_2^{I^*} & \Omega^{I} & -\omega_y & 0 & 0 & 0 & -k_{off} & 0 & 0 \\ 0 & 0 & -k_{FI} & 0 & -\Omega^{I} & R_2^{I^*} & \omega_x & 0 & 0 & 0 & 0 & -k_{off} & 0 \\ -2\Theta^{I} & 0 & 0 & -k_{FI} & \omega_y & -\omega_x & R_1^{I^*} & 0 & 0 & 0 & 0 & 0 & -k_{off} \\ 0 & -k_{on}^{app} & 0 & 0 & 0 & 0 & 0 & R_2^{F\text{-}G^*} & \Omega^{F\text{-}G} & -\omega_y & -k_{IF}^{G} & 0 & 0 \\ 0 & 0 & -k_{on}^{app} & 0 & 0 & 0 & 0 & -\Omega^{F\text{-}G} & R_2^{F\text{-}G^*} & \omega_x & 0 & -k_{IF}^{G} & 0 \\ -2\Theta^{F\text{-}G} & 0 & 0 & -k_{on}^{app} & 0 & 0 & 0 & \omega_y & -\omega_x & R_2^{F\text{-}G^*} & 0 & 0 & -k_{IF}^{G} \\ 0 & 0 & 0 & 0 & -k_{on}^{app} & 0 & 0 & -k_{FI}^{G} & 0 & 0 & R_2^{I\text{-}G^*} & \Omega^{I\text{-}G} & -\omega_y \\ 0 & 0 & 0 & 0 & 0 & -k_{on}^{app} & 0 & 0 & -k_{FI}^{G} & 0 & -\Omega^{I\text{-}G} & R_2^{I\text{-}G^*} & \omega_x \\ -2\Theta^{I\text{-}G} & 0 & 0 & 0 & 0 & 0 & -k_{on}^{app} & 0 & 0 & -k_{FI}^{G} & \omega_y & -\omega_x & R_2^{I\text{-}G^*} \end{bmatrix}\begin{bmatrix} E/2 \\ I_x^{F} \\ I_y^{F} \\ I_z^{F} \\ I_x^{I} \\ I_y^{I} \\ I_z^{I} \\ I_x^{F\text{-}G} \\ I_y^{F\text{-}G} \\ I_z^{F\text{-}G} \\ I_x^{I\text{-}G} \\ I_y^{I\text{-}G} \\ I_z^{I\text{-}G} \end{bmatrix}, \quad \textbf{[S10]}$$

where $R_2^{F^*} = R_2^{F} + k_{FI} + k_{on}^{app}$, $R_2^{I^*} = R_2^{F} + k_{IF} + k_{on}^{app}$, $R_2^{F\text{-}G^*} = R_2^{F\text{-}G} + k_{FI}^{G} + k'_{off}$, and $R_2^{I\text{-}G^*} = R_2^{I\text{-}G} + k_{IF}^{G} + k_{off}$ and similarly for $R_1^{F^*}$, $R_1^{I^*}$, $R_1^{F\text{-}G^*}$, and $R_1^{I\text{-}G^*}$ (replacing $R_2$ by $R_1$ in these definitions). Here, $I$ represents the magnetization of a $^{15}$N nucleus in the rotating frame in the free and GroEL-bound states (denoted by superscripts). $R_1^n$ and $R_2^n$ are (intrinsic) longitudinal and transverse magnetization relaxation rates, respectively, of state $n$ in the absence of exchange; $\Omega^n$ is the difference between the resonant frequency of state $n$ and the frequency of the applied saturation field; $\omega$ is strength of the continuous-wave (CW) saturation field about the given axis ($x$ or $y$); $E$ is unity; and $\Theta^n = R_1^n I_z^n$, where $I_z^n$ is the equilibrium longitudinal magnetization of state $n$. The initial magnetization is entirely longitudinal for the DEST experiment and transverse for the $\Delta R_2$ experiment. The DEST and $\Delta R_2$ experimental data originating from all SH3$^{WT}$ and SH3$^{Mut}$ samples (i.e., $^{15}$N DEST and $^{15}$N-$\Delta R_2$ data for SH3$^{WT/Mut}$ with both labeling schemes, and $^{13}$C$_{methyl}$ DEST, $^{13}$C$_{methyl}$ $\Delta R_2$ data for the [$^{15}$N/$^{1}$H$_N$/AILV-$^{13}$C$_{methyl}$]/deuterated sample) were analyzed in the same manner as briefly outlined below.

The DEST experimental observables, $\kappa$, namely the ratio of the signal intensity of each resonance as a function of saturation offset and saturation field to that without saturation, were calculated as described previously (18, 35). Briefly, the numerical solution for $I_z^n$ after the CW saturation time at each combination of saturation offset $\Omega$, saturation field $\omega_x$, and residue position is calculated as a function of saturation offset by solving Eq. **S10** using matrix exponentiation. The value of $\kappa$ was computed by calculating the difference between two initial conditions of $^{15}$N magnetization (aligned either along $+z$ or $-z$ axes: $I_{+z}$ and $I_{-z}$), $I_{+z} - I_{-z}$, and subsequently normalized to the solution without saturation. Experimentally determined $R_1^n$ and $R_2^n$ values for states **F** and **I** (assumed the same) were supplied to the fitting procedure, whereas $R_1^n$ values for the bound states (**I-G** and **F-G**) were set to a constant value of 0.05 s$^{-1}$. As noted earlier, the exact value of $R_1$ does not affect the results by design of the experiment (18). For the purposes of fitting the $^{15}$N-DEST data, one can also readily assume that the $^{15}$N chemical shifts in the free and bound states are equal ($\Omega^{F} = \Omega^{I} = \Omega^{F\text{-}Gr} = \Omega^{I\text{-}Gr}$) because any shift differences are very small compared with the width of the DEST saturation profiles (18, 35).

$\Delta R_2$ values for SH3$^{Mut}$ in the presence of GroEL (SH3$^{Mut}$ + GroEL, the second term in Eq. **S3**) were calculated by propagating Eq. **S9** with $\omega_{x,y} = 0$ and initial magnetization along one of the transverse axes (e.g., $x$), using a simple two-time-point single-exponential decay,

$$\Delta R_2 = \frac{\ln\left[I_x^{F}(\tau_1)/I_x^{F}(\tau_2)\right]}{\tau_2 - \tau_1} - R_2^{F}, \quad \textbf{[S11]}$$

where the delays $\tau_1$ and $\tau_2$ were set to 10 ms and 100 ms, respectively. $\tau_1$ was chosen to remove any small deviations from exponential behavior at very short delays and $\tau_2$ to match the order of magnitude of the experimental delays used to measure $R_2$. For the

fitting of $\Delta R_2$, all of the states were assumed to have the same chemical shifts as contributions to $R_2$ arising from chemical exchange are for all practical purposes completely suppressed in $R_{1\rho}$ measurements. $\Delta R_2$ values for the $SH3^{WT}$ data (the first term in Eq. **S3**) were calculated in a similar manner, using a simple two-state model.

## SI Materials and Methods

**Expression and Purification of SH3 Domains.** Plasmids encoding the wild type ($SH3^{WT}$) and triple mutant (A39V/N53P/V55L, $SH3^{Mut}$) of the *Gallus gallus* Fyn SH3 domain (T85-D142, corresponding to residues 2–59 in this paper) were constructed as previously described (14, 15), codon optimized, and synthesized by Genscript. The plasmids had an N-terminal $His_6$ Tag and tobacco etch virus (TEV) protease (36), cleavage site positioned such that the final protein product retains the sequence GAMVQIS at the N terminus and a C-terminal Arg residue. The resulting constructs were cloned into pET21a expression plasmids and expressed in BL21 Star (DE3) *Escherichia coli* cells (Life Technologies). Purification of each construct was identical and was based on the protocol described previously (37). Briefly, *E. coli* cells containing the expression plasmids for the SH3 domains were grown at 37 °C in M9 minimal medium supplemented with the relevant nitrogen, carbon, and biosynthetic precursors until an $A_{600} \sim 0.6$; induced with 0.5 mM isopropyl β-D-1-thiogalactopyranoside (IPTG); and grown for an additional 4 h. Cells were harvested by centrifugation (4,000 × *g* for 15 min), resuspended in buffer A (6 M GdnHCl, 50 mM sodium phosphate, pH 8.0, 500 mM NaCl, 10 mM imidazole, and EDTA-free protease inhibitor mixture) (Roche Life Science), and lysed by two passes through a high-pressure homogenizer (Avestin). The resulting lysate was cleared (40,000 × *g* for 25 min), filtered (0.45 μm), passed over a 5-mL HisTrap FF column (GE Healthcare), and eluted with buffer A containing 400 mM imidazole. Eluted fractions containing protein were pooled, diluted to ∼1 mg/mL protein concentration, and dialyzed against 2 × 4 L 50 mM Tris, pH 8.0, 1 mM EDTA, 2 mM DTT. The dialysis buffer was changed a third time and TEV (1 $A_{280}$ TEV to ∼20 $A_{280}$ target) was added and the reaction was kept at 4 °C for 18 h. Postdialysis, TEV-digested SH3 was cleared (10,000 × *g* for 10 min), the EDTA was neutralized by the addition of an equimolar amount of $MgCl_2$, and it was applied to a freshly $Ni^{2+}$-charged 5-mL HisTrap FF column. The flow through was collected, concentrated (3,500 molecular weight cutoff centrifugal filter) (Millipore), and applied to a Superdex 75 HiLoad size exclusion column (GE Healthcare). Purified SH3 domains were concentrated to ∼1.5 mM, exchanged into NMR buffer [50 mM sodium phosphate, pH 7.0, 0.2 mM EDTA, 0.05% (wt/vol) $NaN_3$, 10% (vol/vol) $D_2O$], and stored at 4 °C.

Four NMR samples of the SH3 domains were used in the current work: (*i*) protonated and uniformly $^{15}N$-labeled $SH3^{WT}$ and $SH3^{Mut}$ using $^{15}NH_4Cl$ and protonated glucose as the sole nitrogen and carbon sources, respectively, in $H_2O$-based M9 minimal medium, [U-$^{15}N$]-$SH3^{WT}$/$SH3^{Mut}$ (referred to hereafter as $^{15}N$/protonated-SH3); and (*ii*) perdeuterated $SH3^{WT}$ and $SH3^{Mut}$ with selective $^{13}CH_3$ labeling of Ala-β, Ile-$\delta_1$, Leu-δ, and Val-γ (AILV) methyl groups obtained using $^{15}NH_4Cl$ as the nitrogen source, [U-$^2$H]-glucose as the carbon source, and the appropriate set of biosynthetic precursors added to $D_2O$-based M9 minimal medium before induction as described previously (38), [$^{15}N/^1H_N$, Ala-$^{13}CH_3$, Ile$\delta_1$-$^{13}CH_3$, Leu,Val-$^{13}CH_3/^{12}CD_3$] and otherwise deuterated $SH3^{WT}$/$SH3^{Mut}$ (hereafter referred to as [$^{15}N/^1H_N$/AILV-$^{13}CH_3$]/deuterated-SH3). Note that in the latter pair of samples, $^{13}CH_3$ labeling in the isopropyl moieties of Leu and Val is restricted to one methyl group only, the other remaining $^{12}CD_3$ (39). Isotopic incorporation for each sample was confirmed by liquid chromatography/mass spectrometry.

**GroEL Expression and Purification.** The pGEL1 plasmid expressing GroEL (40) (gift from George Lorimer, University of Maryland, College Park, MD) was transformed into BL21 (DE3) *E. coli* cells, expressed, and purified as previously described (40). Endogenous *E. coli* proteins bound to GroEL after the chromatographic steps were removed with two rounds of acetone precipitation. The purity of GroEL was measured using tryptophan fluorescence (because GroEL has no native tryptophan residues, tryptophan fluorescence is a sensitive measure of the purity of GroEL). Purified GroEL was concentrated to ∼1 mM in subunits, exchanged into NMR buffer, and stored at 4 °C.

**Ribulose-1,5-Bisphosphate Carboxylase Expression and Purification.** The plasmid expressing *Rhodospirillum rubrum* ribulose-1,5-bisphosphate carboxylase (Rubisco) (gift of George Lorimer) (21) was transformed into BL21 (DE3) *E. coli* cells, grown in Luria–Bertani medium, and expressed and harvested identically to the SH3 domains described above. The cell pellet was processed as described for SH3 with the exception that it was resuspended in buffer B (20 mM Tris, pH 8.0, 300 mM NaCl, 10 mM imidazole). The cleared lysate was loaded on a 5-mL HisTrap FF column and eluted with buffer B containing 400 mM imidazole. Fractions containing Rubisco were pooled and dialyzed, and the His Tag was removed by TEV digestion as described above. Post-TEV digestion, the contents of the dialysis bag were cleared (10,000 × *g* for 10 min), concentrated (10,000 molecular weight cutoff centrifugal filter), and loaded onto a Superdex 200 HiLoad size exclusion column (GE Healthcare) equilibrated with 50 mM Tris, 50 mM NaCl, and 1 mM EDTA. Finally, Rubisco-containing fractions were pooled, buffer exchanged into 2 mM Tris, pH 7.4 (G25 HiPrep Desalting column; GE Healthcare), concentrated to ∼500 μM (10,000 molecular weight cutoff centrifugal filter), flash frozen in liquid $N_2$, and stored at −80 °C. Rubisco was acid denatured by mixing equal volumes of Rubisco stock solution and 20 mM HCl (21).

**NMR Sample Preparation.** All $SH3^{Mut}$ and $SH3^{WT}$ samples were prepared in carefully matched pairs (with and without GroEL) to a final volume of 550 μL. An appropriate amount of the SH3 stock solution (equilibrated in NMR buffer) for two samples was diluted into 900 μL NMR buffer [50 mM sodium phosphate, pH 7.0, 0.2 mM EDTA, 0.05% (wt/vol) $NaN_3$, 10% (vol/vol) $D_2O$]. This was subsequently split into two equal fractions and added to either 100 μL of NMR buffer (reference sample) or 100 μL NMR buffer containing 660 μM (in subunits) GroEL. No significant spectral differences were observed in the $^1H$-$^{15}N$ correlation spectra in the presence or absence of GroEL for either $^{15}N$/protonated-$SH3^{WT}$/$SH3^{Mut}$ or [$^{15}N/^1H_N$/AILV-$^{13}CH_3$]/deuterated-$SH3^{WT}$/$SH3^{Mut}$. Rubisco-containing samples were prepared in a similar fashion but the GroEL was first saturated with stoichiometric amounts of acid-denatured Rubisco as described previously, before the addition of SH3 (20).

**NMR Spectroscopy.** All NMR experiments were recorded at 10 °C, using Bruker Avance-III spectrometers operating at $^1H$ frequencies of 900.27 MHz, 800.1 MHz, 600.13 MHz, and 500.1 MHz, each equipped with Bruker TCI *z*-axis gradient cryogenic probes. Temperature differences between spectrometers were corrected by matching the chemical shift difference between residual water and the methyl resonance of 4,4-dimethyl-4-silapentance-1-sulfonic acid (DSS) (0 ppm) in a sample containing 50 mM sodium phosphate, pH 7.0, 0.2 mM EDTA, 0.5% (wt/vol) DSS, 0.05% (wt/vol) $NaN_3$, and 99.9% (vol/vol) $D_2O$.

**$^{15}N$ and $^{13}C_{methyl}$ Relaxation Measurements.** $^{15}N$-$R_{1\rho}$ and $^{15}N$-$R_1$ measurements were carried out using heat-compensated, $^{15}N$ heteronuclear single-quantum coherence (HSQC)-based pulse schemes (41) on samples of $SH3^{WT}$ and $SH3^{Mut}$ containing 100 μM of protein in the absence and presence of 120 μM (in subunits) GroEL and in the presence of 120 μM GroEL and 19 μM

acid-denatured Rubisco. An effective spin-lock field of 1.8 kHz was used in the $^{15}$N-$R_{1\rho}$ experiments to completely suppress chemical exchange-induced line broadening. The following relaxation delays were used in the $^{15}$N-$R_{1\rho}$ experiments: 1 ms, 21 ms, 41 ms, 71 ms, 111 ms, and 150 ms at 600 MHz and 1 ms, 21 ms, 41 ms, 61 ms, 81 ms, and 100 ms at 900 MHz. The relaxation delays for the $^{15}$N-$R_1$ experiments were as follows: 0 ms, 120 ms, 200 ms, 320 ms, 520 ms, and 720 ms at 600 MHz and 0 ms, 160 ms, 320 ms, 520 ms, 720 ms, and 1,000 ms at 900 MHz. Each 2D experiment was composed of 80* × 512* (600 MHz) or 80* × 1,024* (900 MHz) complex points in the indirect ($^{15}$N) and direct ($^{1}$H) dimensions, respectively, corresponding to respective acquisition times of 53 ms and 58 ms at 600 MHz and 35 ms and 81 ms at 900 MHz. Experiments were acquired with 32 scans per free induction decay (FID) and an interscan delay of 1.5 s, resulting in net acquisition times of ∼18 h per experiment.

$^{13}C_{methyl}$-$R_{1\rho}$ and $^{13}C_{methyl}$-$R_1$ measurements were carried out on the samples of 100 μM [$^{15}$N/$^{1}H_N$/AILV-$^{13}CH_3$]/deuterated SH3$^{Mut}$ and SH3$^{WT}$ at 600 MHz and 800 MHz, using straightforward modifications of the pulse schemes described by Kay et al. (42) to ensure that only in-phase $^{13}$C coherences ($C_{x,y}$ or $C_z$) decay during the relaxation periods and to optimize for detection of methyl groups (43). Fast application of 125° $^{1}$H pulses during the relaxation period of $^{13}C_{methyl}$-$R_{1\rho}$ measurements ensures that the decay of the signal is nearly single exponential (44, 45). Note that the field dependence of methyl $^{13}$C relaxation rates is very weak, with the values obtained at 600 MHz only 4–5% lower on average that those obtained at 800 MHz. An effective spin-lock field of 2.0 kHz was used in $^{13}$C-$R_{1\rho}$ measurements to suppress chemical exchange-induced line broadening. The following respective relaxation delays were used in the $^{13}C_{methyl}$-$R_{1\rho}$ and $R_1$ experiments at both 600 MHz and 800 MHz: 0 ms, 80 ms, 160 ms, 240 ms, 280 ms, and 400 ms, and 0 ms, 40 ms, 80 ms, 120 ms, 160 ms, and 200 ms. Each 2D experiment comprised 80* × 512* (750*) complex points in the indirect ($^{13}C_{methyl}$) and direct ($^{1}H^{methyl}$) dimensions, respectively, corresponding to respective acquisition times of 31 (23) ms and 61 (67) ms, respectively (where the values in parentheses refer to the experiments at 800 MHz). Experiments were acquired with 32 scans per FID and an interscan delay of 1.5 s, resulting in net acquisition times of ∼18 h per experiment.

The spectra were processed and the relaxation decays were best fit to a single exponential function $Ae^{-RT}$, where $R$ is a relaxation rate and $T$ the relaxation delay, using the nmrPipe/nmrDraw software suite (46). Errors in the extracted rates were estimated via extensive Monte Carlo simulations. $^{15}$N/$^{13}$C-$R_2$ (in-phase) values were calculated from the extracted $^{15}$N/$^{13}$C-$R_{1\rho}$ and $^{15}$N/$^{13}$C-$R_1$ values, using the relationship $R_2 = [R_{1\rho} - R_1 \cos^2\theta]/\sin^2\theta$, where $\theta$ is the angle subtended by the effective spin-lock field with respect to the external magnetic field. $\Delta R_2$ values were subsequently calculated as the differences between the $R_2$ rates in the presence of GroEL (or GroEL+Rubisco) and in the absence of GroEL, with appropriate propagation of errors.

**$^{15}$N- and $^{13}C_{methyl}$-DEST Spectroscopy.** $^{15}$N-DEST experiments using the pulse scheme described previously (18, 35) were carried out at 900 MHz on samples containing 100 μM $^{15}$N/protonated-SH3$^{Mut}$/SH3$^{WT}$ or [$^{15}$N/$^{1}H_N$/AILV-$^{13}CH_3$]/deuterated-SH3$^{Mut}$ in the presence of 120 μM (in subunits) GroEL, using $^{15}$N saturation field strengths of 500 Hz and 750 Hz for a total duration of 0.7 s. A set of 19 offsets from the $^{15}$N carrier frequency (±15 kHz, ±10 kHz, ±8 kHz, ±7 kHz, ±6 kHz, ±5 kHz, ±4 kHz, ±2 kHz, ±1 kHz, 0 kHz) were used at both saturation field strengths and supplemented by two control experiments with offsets of 15 kHz and a continuous-wave (CW) field of 0 Hz. $^{13}C_{methyl}$-DEST experiments on 100 μM [$^{15}$N/$^{1}H_N$/AILV-$^{13}CH_3$]/deuterated-SH3$^{Mut}$/SH3$^{WT}$ in the presence of 120 μM (in subunits) GroEL were performed at 600 MHz, using an appropriately modified pulse scheme reported previously (45) to account for the absence of uniform $^{13}$C labeling and to optimize for detection of methyl groups as described elsewhere (43). $^{13}$C saturation field strengths of 750 Hz and 1,500 Hz for a total duration of 0.4 s were applied at 25 different offsets from the $^{13}$C carrier frequency (±20 kHz, ±15 kHz, ±12 kHz, ±10 kHz, ±8 kHz, ±7 kHz, ±6 kHz, ±5 kHz, ±4 kHz, ±3 kHz, ±2 kHz, ±1 kHz, 0 kHz). Processing of the 2D $^{15}$N- and $^{13}C_{methyl}$-DEST data closely followed that of our earlier studies (20). DEST profiles were extracted from the ratio of cross-peak heights in the experiments with saturation to the height(s) of the corresponding cross-peaks in the reference experiment(s) without saturation.

For $^{15}$N-DEST, each 2D experiment comprised 80* × 1,024* complex points in the indirect ($^{15}$N) and direct ($^{1}$H) dimensions, respectively, corresponding to respective acquisition times of 35 ms and 95 ms. Experiments were acquired with 32 scans per FID and an interscan delay of 1.6 s, resulting in net acquisition times of ∼3 d per $^{15}$N-DEST experiment. For $^{13}C_{methyl}$-DEST, each 2D experiment comprised 80* × 512* complex points in the indirect ($^{13}C_{methyl}$) and direct ($^{1}H_{methyl}$) dimensions, respectively, corresponding to respective acquisition times of 81 ms and 61 ms. Experiments were acquired with 48 scans per FID and an interscan delay of 1.0 s, resulting in net acquisition times of ∼3.4 d per $^{13}C_{methyl}$-DEST experiment.

**Relaxation Dispersion Measurements.** $^{15}$N relaxation dispersion experiments were acquired using a $^{15}$N-CPMG (47) scheme with amide proton decoupling ($^{1}H_N$-CW $^{15}$N-CPMG) (48) at 600 MHz and 900 MHz on 100-μM $^{15}$N/protonated-SH3$^{Mut}$ and [$^{15}$N/$^{1}H_N$/AILV-$^{13}CH_3$]/deuterated-SH3$^{Mut}$ samples in the presence of 120 μM (in subunits) GroEL and on both 100 μM and 1 mM $^{15}$N/protonated-SH3$^{Mut}$ and [$^{15}$N/$^{1}H_N$/AILV-$^{13}CH_3$]/deuterated-SH3$^{Mut}$ in the absence of GroEL. (No relaxation dispersion was observed for SH3$^{WT}$ in the absence or presence of GroEL.) Typical CPMG field strengths, $\nu_{CPMG}$, of 0 Hz, 20 Hz, 40 Hz, 60 Hz, 80 Hz, 100 Hz, 120 Hz, 140 Hz, 160 Hz, 180 Hz, 200 Hz, 220 Hz, 240 Hz, 280 Hz, 320 Hz, 360 Hz, 400 Hz, 440 Hz, 480 Hz, 520 Hz, 560 Hz, 640 Hz, 720 Hz, 800 Hz, 900 Hz, and 1,000 Hz, where $\nu_{CPMG} = 1/(2\tau_{CP})$, and $\tau_{CP}$ is the time between 180° $^{15}$N-CPMG pulses, were applied for a constant $^{15}$N relaxation period of 50 ms. $^{1}H_N$-CW decoupling was applied at a radiofrequency (RF) field strength of 11 kHz. The experiment recorded with the relaxation period omitted served as a reference for the calculation of effective $R_2$ rates as a function of $\nu_{CPMG}$ field strength as described previously (48). Note that the $^{15}$N-CPMG scheme with $^{1}H_N$-CW decoupling effectively measures the relaxation rates of in-phase $^{15}$N coherences (as is the case when $R_2$ is measured using the $R_{1\rho}$ experiment) and allows the use of an odd number of CPMG cycles during each half of the constant relaxation period (48). Each 2D $^{15}$N-relaxation dispersion experiment comprised 80* × 1,024* complex points at 900 MHz and 80* × 512* complex points at 600 MHz in the indirect ($^{15}$N) and direct ($^{1}$H) dimensions, respectively, corresponding to respective acquisition times of 35 ms and 71 ms at 900 MHz and 53 ms and 61 ms at 600 MHz. Experiments were acquired with 48 scans per FID and an interscan delay of 2.0 s, resulting in net acquisition times of ∼4.5 d per experiment.

Amide proton ($^{1}H_N$) relaxation dispersion experiments were acquired using the $^{1}H_N$-CPMG scheme of Ishima and Torchia (49) on 100 μM [$^{15}$N/$^{1}H_N$/AILV-$^{13}CH_3$]/deuterated-SH3$^{Mut}$ in the presence of 120 μM (in subunits) GroEL and on both 100 μM and 0.5 mM [$^{15}$N/$^{1}H_N$/AILV-$^{13}CH_3$]/deuterated-SH3$^{Mut}$ in the absence of GroEL. Sixteen values of $^{1}$H $\nu_{CPMG}$ ranging from 0 Hz to 2,000 Hz were used: 0 Hz, 100 Hz, 200 Hz, 300 Hz, 400 Hz, 500 Hz, 600 Hz, 700 Hz, 800 Hz, 900 Hz, 1,000 Hz, 1,200 Hz, 1,400 Hz, 1,600 Hz, 1,800 Hz, and 2,000 Hz. A constant $^{1}H_N$ relaxation period of 40 ms was used, with the remaining spectral parameters as in $^{15}$N relaxation dispersion experiments. Note that deuteration is indispensable for successful recording of $^{1}H_N$ relaxation dispersions in proteins (49, 50). Each 2D $^{1}H_N$ relaxation dispersion experiment at 600 (and 800) MHz comprised 80* × 512* (750*) complex points in

the indirect ($^{15}$N) and direct ($^{1}$H) dimensions, respectively, corresponding to respective acquisition times of 53 (40) ms and 66 (67) ms. Experiments were acquired with 48 (32) scans per FID and an interscan delay of 1.7 s, resulting in net acquisition times of ~2.8 (1.8) d per experiment (49).

SQ $^{13}C_{methyl}$ relaxation dispersion experiments were recorded at 600 MHz and 800 MHz on 100 μM [$^{15}N/^{1}H_N$/AILV-$^{13}CH_3$]/deuterated-SH3$^{Mut}$ in the absence and presence of 120 μM (in subunits) GroEL, using the pulse scheme of Lundstrom et al. (51). The following values of $^{13}C$ $\nu_{CPMG}$ field were used: 0 Hz, 50 Hz, 100 Hz, 150 Hz, 200 Hz, 250 Hz, 300 Hz, 350 Hz, 400 Hz, 450 Hz, 500 Hz, 550 Hz, 600 Hz, 650 Hz, 700 Hz, 800 Hz, 900 Hz, and 1,000 Hz. A constant $^{13}C$ relaxation time of 40 ms was used, with the rest of the spectral parameters as in the $^{13}C_{methyl}$ relaxation experiments as described above. Each 2D $^{13}C_{methyl}$ relaxation dispersion experiment was acquired with 32 scans per FID and an interscan delay of 1.5 s, resulting in net acquisition times of ~1.8 d per experiment.

**Diffusion Measurements.** NMR diffusion experiments were performed at 600 MHz on 100-μM solutions of $^{15}$N/protonated-SH3$^{Mut}$ in the absence and presence of 120 μM (in subunits) GroEL, using the 2D $^{1}$H-$^{15}$N correlation experiment of Bodenhausen and coworkers (52) and repeated with the scheme of Choy et al. (53). Essentially identical measures of diffusion were obtained in the samples with and without GroEL from the fitting of cross-peak intensities as a function of pulsed-field gradient strengths, from which one can infer that the transverse relaxation properties and rotational correlation time of unbound SH3 (i.e., the NMR visible species) are unaffected by the presence of GroEL. This was also verified by analytical ultracentrifugation that demonstrated the existence of only two different molecular weight species, one corresponding to free SH3 and the other to GroEL (i.e., there was no evidence for aggregation of either SH3 or GroEL).

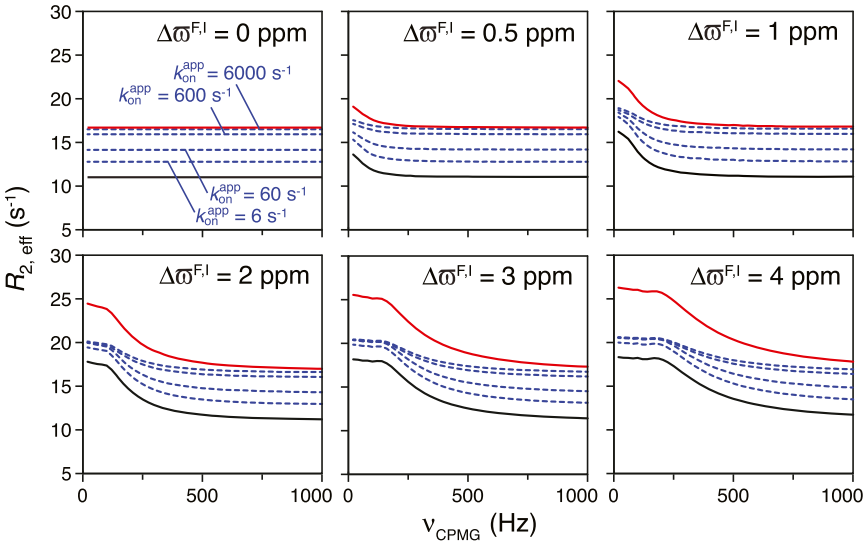


**Fig. S1.** In the absence of exchange between the F-G and I-G states, relaxation dispersion and $\Delta R_2$ cannot be accounted for simultaneously in the presence of GroEL. Each panel shows the same simulations for different values of $\Delta\varpi^{F,I} = \Delta\varpi^{F,I-G}$ (i.e., $\Delta\varpi^{I,I-G} = 0$; note that in the absence of a fast exchange process connecting I-G to F via F-G, $\Delta\varpi^{I,I-G}$ has minimal impact on the relaxation dispersion profiles). Black curves show relaxation dispersions calculated for a two-state system with the interconversion between F and I states with $k_{FI}$ and $k_{IF}$ set to the experimentally determined values of 7.5 s$^{-1}$ and 310 s$^{-1}$, respectively (compare with Table 1 in main text). Red curves show relaxation dispersions calculated using the four-state model and parameters (rate constants and $R_2$ rates) shown in Fig. 2 of the main text (compare with Tables 2 and 3 in main text). Blue curves show relaxation dispersions for a four-state model where the F-G and I-G states do not directly interconvert with one another (i.e., $k_{FI}^{G} = k_{IF}^{G} = 0$), $k_{on}^{app} = 6$ s$^{-1}$, 60 s$^{-1}$, 600 s$^{-1}$, and 6,000 s$^{-1}$, and the population of the I-G state I, $p_{I\text{-}G}$, is kept constant by scaling the $k_{off}$ proportionately (i.e., $k_{off} = 20$ s$^{-1}$, 200 s$^{-1}$, 2,000 s$^{-1}$, and $2 \times 10^4$ s$^{-1}$), and the remaining rate constants and $R_2$ values are set to the same values as in the red curves. Experimentally, the dispersion profiles in the presence of GroEL are shifted by the $\Delta R_2$ value while retaining similar shapes (compare black vs. red simulated curves). In the absence of interconversion between the F-G and I-G states (blue curves), varying the association rate constant $k_{on}^{app}$ for the binding of F and I to GroEL does not reproduce the experimental observations, indicating that interconversion between F-G and I-G states is required.

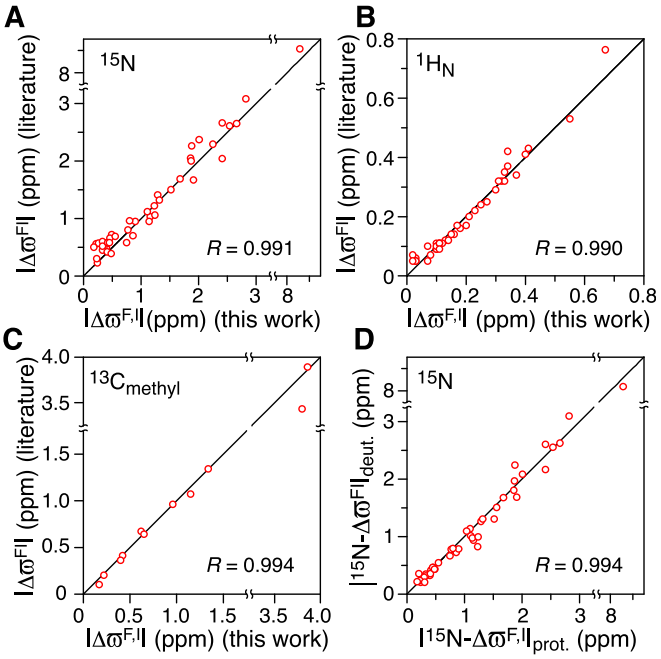


**Fig. S2.** Chemical shift difference comparisons between the free F and I states. Comparison of absolute chemical shift differences between the free F and I states ($|\Delta\varpi^{F,I}|$) is determined here from the global fits (*x* axis) and those reported in the literature by Neudecker et al. (14) (*y* axis) for (*A*) $^{15}$N, (*B*) $^{1}H_N$, and (*C*) $^{13}C_{methyl}$ nuclei. Also shown in *D* is the correlation between the $|^{15}N\text{-}\Delta\varpi^{F,I}|$ values obtained in the present work for the $^{15}$N/protonated (*x* axis) and [$^{15}N/^{1}H_N$/AILV-$^{13}CH_3$]/deuterated (*y* axis) SH3$^{Mut}$ samples. The Pierson correlation coefficient *R* is also listed.

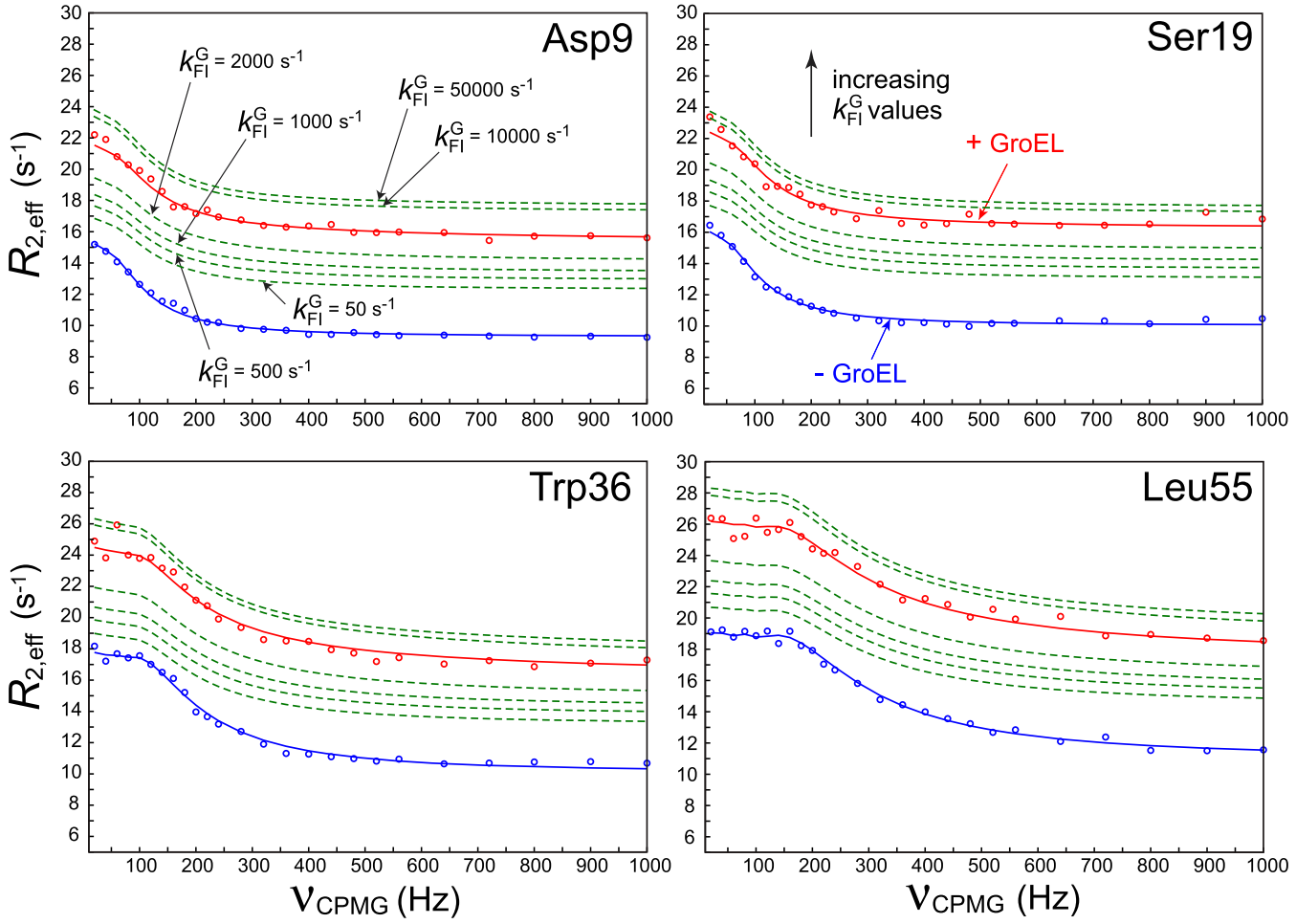


**Fig. S3.** The experimental relaxation dispersion profiles and $\Delta R_2$ values in the presence of GroEL are consistent with an acceleration in the interconversion rates between the F and I states only upon binding GroEL. The four panels show comparisons of experimental and simulated $^{15}$N-CPMG relaxation dispersion profiles at a spectrometer frequency of 900 MHz for the same residues (Asp9, Ser19, Trp36, and Leu55) shown in Fig. 2 of the main text. The experimental data for SH3$^{Mut}$ in the absence and presence of GroEL are displayed as blue and red circles, respectively. The corresponding calculated curves obtained from the global best-fitting procedure to kinetic scheme 1 (Eq. **S1**) with the optimized values of the rate constants (Table 2 of main text; the optimized values of the interconversion rate constants between the F and I states when bound to GroEL are $k_{FI}^G = 4{,}000$ s$^{-1}$ and $k_{FI}^G = 1{,}300$ s$^{-1}$), bound $R_2$ values, and $\Delta\omega$ values (*SI Theory*) are shown as solid blue and red lines, respectively. Simulated CPMG profiles are shown as green dashed lines for values of $k_{FI}^G$ ranging from 50 s$^{-1}$ to 50,000 s$^{-1}$, as indicated at *Top Left*. The $k_{FI}^G/k_{IF}^G$ ratio is kept constant at a value of 3.077 (the value obtained from the global best fit) to maintain detailed balance (see Eq. **S2**). The shape of the profiles, the $R_{ex}$ values (the difference in $R_2$ at 0-Hz and 1,000-Hz CPMG field), and the $\Delta R_2$ values (the difference in $R_2$ in the presence and absence of GroEL at a CPMG field of 1,000 Hz where exchange contributions to $R_{2,eff}$ are suppressed) are reproduced only with the values of $k_{FI}^G$ and $k_{IF}^G$ provided in Table 2. For values of $k_{FI}^G$ and $k_{IF}^G$ smaller than the optimized ones, the calculated values of both $R_{ex}$ and $\Delta R_2$ are too small; for values of $k_{FI}^G$ and $k_{IF}^G$ larger than the optimized ones, the calculated values of $\Delta R_2$ are too large.

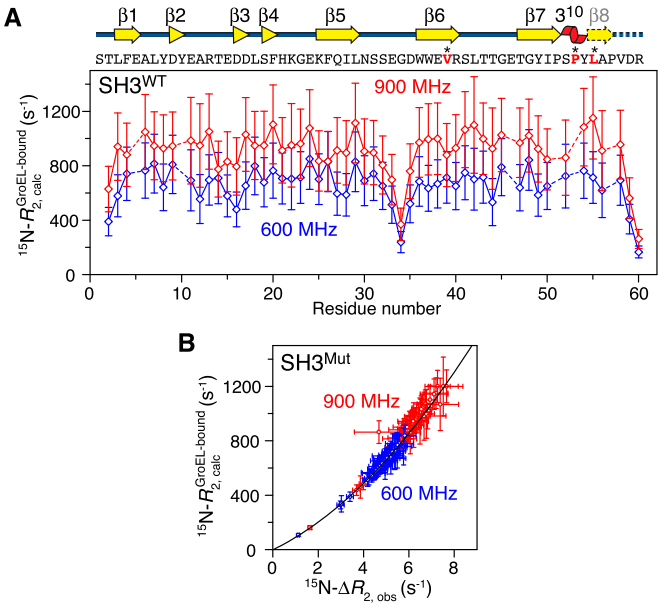


**Fig. S4.** Transverse relaxation rates of SH3 bound to GroEL. (*A*) Calculated $^{15}$N-$R_2^{bound}$ profile for SH3$^{WT}$ bound to GroEL [state F-G at 900 (red) MHz and 600 (blue) MHz]. (*B*) Correlation between calculated $^{15}$N-$R_2^{bound}$ values for the I-G state and the measured $^{15}$N-$\Delta R_2$ values for SH3$^{Mut}$. Experiments were conducted at 10 °C. Error bars: 1 SD.

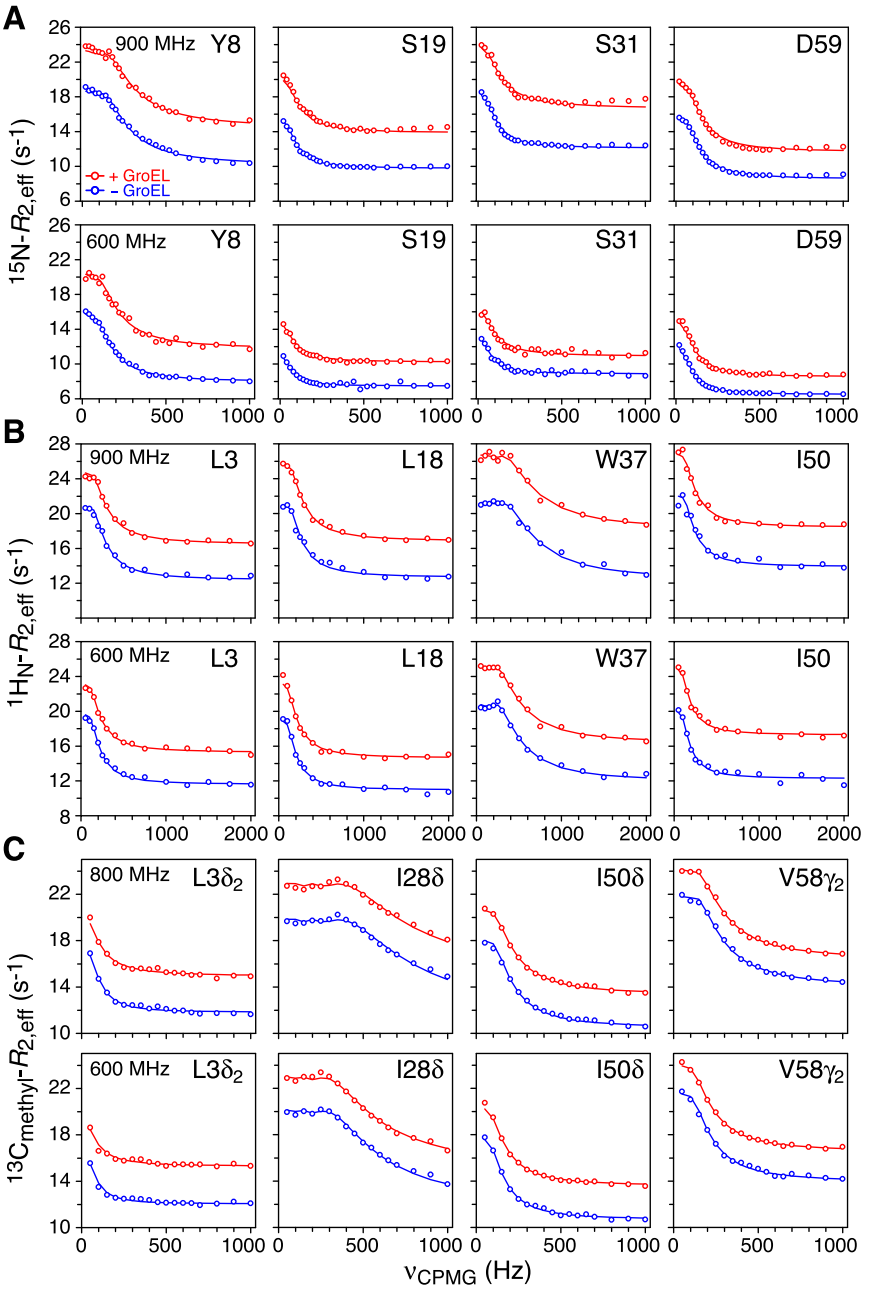


**Fig. S5.** CPMG relaxation dispersion data for the [$^{15}$N/$^{1}$H$_N$/AILV-$^{13}$CH$_3$]/deuterated-SH3$^{Mut}$ sample in the presence and absence of GroEL. (*A*–*C*) Examples of experimental (circles) and best-fit (lines) CPMG relaxation dispersion profiles for (*A*) $^{15}$N, (*B*) $^{1}$H$_N$, and (*C*) $^{13}$C$_{methyl}$ as a function of CPMG field strength ($\nu_{CPMG}$) in the presence (red, 120 μM in subunits) and absence (blue) of GroEL at 900 MHz (800 MHz for $^{13}$C$_{methyl}$) (*A*–*C*, *Top rows*) and 600 MHz (*A*–*C*, *Bottom rows*). All experiments were conducted at 10 °C.

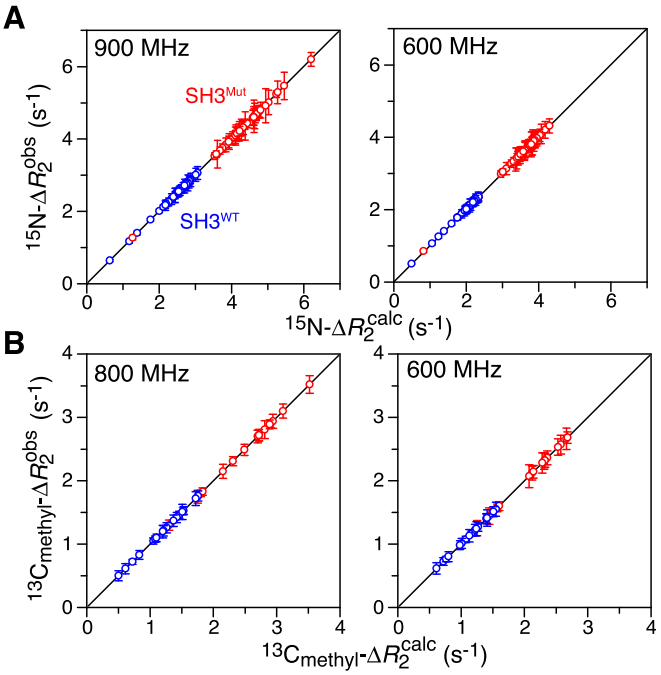


**Fig. S6.** Comparison of observed and calculated $\Delta R_2$ values for [$^{15}$N/$^{1}$H$_N$/AILV-$^{13}$C$_{methyl}$]/deuterated-SH3$^{Mut}$ in the presence of GroEL. (*A*) $^{15}$N-$\Delta R_2$ at 900 MHz (*Left*) and 600 MHz (*Right*). (*B*) $^{13}$C$_{methyl}$-$\Delta R_2$ at 800 MHz (*Left*) and 600 MHz (*Right*).

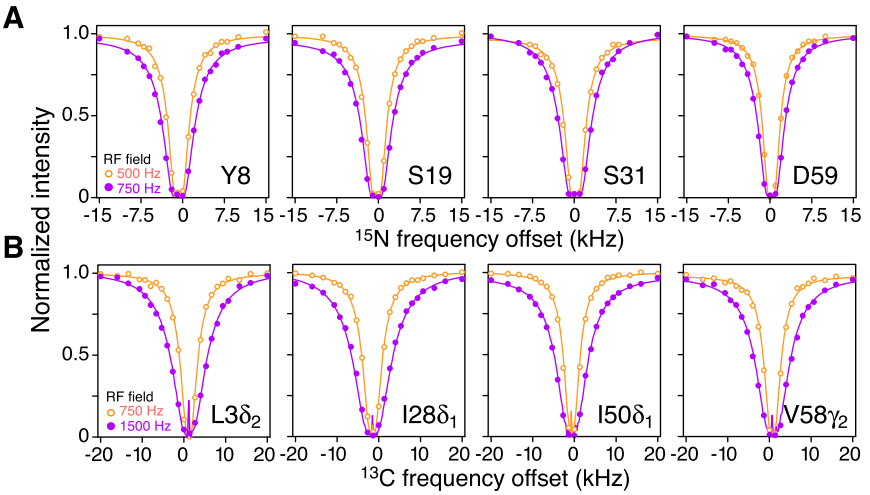


**Fig. S7.** $^{15}$N- and $^{13}$C$_{methyl}$-DEST profiles recorded on [$^{15}$N/$^{1}$H$_N$/AILV-$^{13}$CH$_3$]/deuterated-SH3$^{Mut}$ in the presence of GroEL. (*A* and *B*) Examples of experimental (circles) and best-fit (lines) DEST profiles for (*A*) $^{15}$N and (*B*) $^{13}$C$_{methyl}$ as a function of frequency offset from the $^{15}$N (119.5 ppm) and $^{13}$C (18 ppm) carrier, respectively. Data were recorded at two RF field strengths: 500 Hz (orange) and 750 Hz (purple) for $^{15}$N and 750 Hz (orange) and 1,500 Hz (purple) for $^{13}$C. All experiments were conducted at 10 °C.

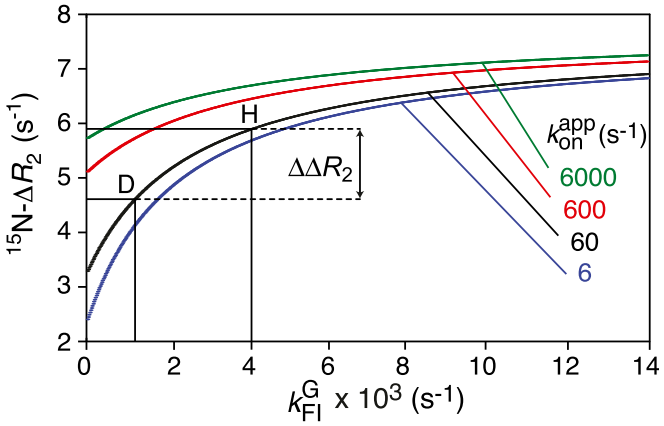


**Fig. S8.** Effect of the value of the rate constant $k_{FI}^{G}$ on $\Delta R_2$. Shown are plots of simulated $^{15}$N-$\Delta R_2$ as a function of $k_{FI}^{G}$ for $k_{on}^{app}$ = 6 s$^{-1}$, 60 s$^{-1}$, 600 s$^{-1}$, and 6,000 s$^{-1}$. The population of the GroEL-bound I-G state, $p_{I\text{-}G}$, is kept constant by scaling the rate constant $k_{off}$ proportionately ($k_{off}$ = 20 s$^{-1}$, 200 s$^{-1}$, 2,000 s$^{-1}$, and 2 × 10$^4$ s$^{-1}$), and the remaining rate constants and bound $R_2$ values are as listed in Tables 2 and 3 of the main text, respectively. $\Delta\Delta R_2$ represents the decrease in $\Delta R_2$ between the protonated ("H") sample and its deuterated counterpart ("D").

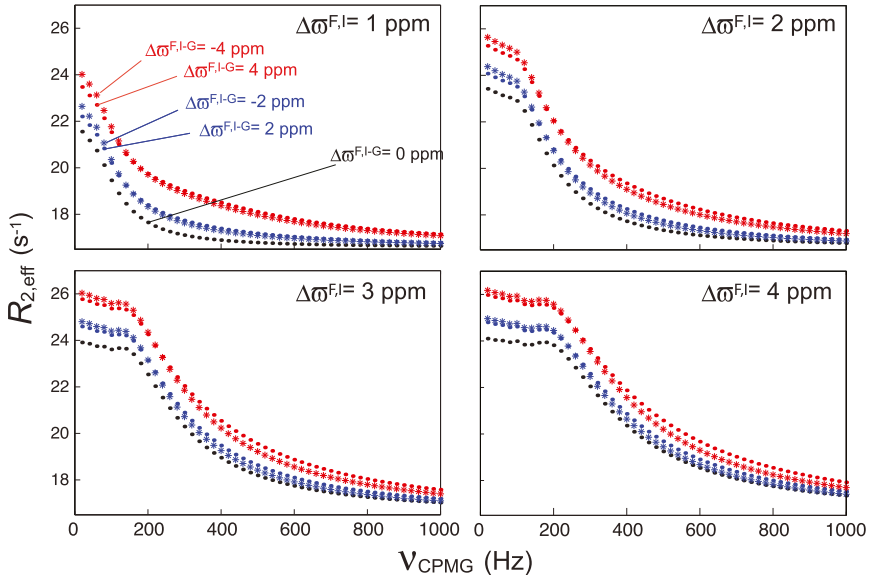


**Fig. S9.** Effect of the sign of $\Delta\varpi^{F,I-G}$ on the $^{15}$N relaxation dispersion profiles. $^{15}$N profiles are simulated for the four-state exchanging system shown in Fig. 3 of the main text (as well as in Eq. **S1** of *SI Theory*), using the rate constants and populations for $^{15}$N-SH3$^{Mut}$ listed in Table 2 of the main text for $\Delta\varpi^{F,I}$ = 1 ppm, 2 ppm, 3 ppm, and 4 ppm at a $^1$H spectrometer frequency of 900 MHz. In each case, the profiles shown with black circles are calculated for $\Delta\varpi^{F,I-G}$ = 0 ppm; the profiles shown with blue circles and asterisks are calculated for $\Delta\varpi^{F,I-G}$ = +2 ppm and −2 ppm, respectively; and the profiles shown with red circles and asterisks are calculated for $\Delta\varpi^{F,I-G}$ = +4 ppm and −4 ppm, respectively.